Second-order wave drift loads on floating structures with thin perforated shells

Peiwen Cong [1], Hui Liang [2,*], Yingyi Liu [3], and Bin Teng [1]

[1] *State Key Laboratory of Coastal and Offshore Engineering, Dalian University of Technology, Dalian 116024, China*

[2] *Technology Centre for Offshore and Marine, Singapore (TCOMS), 118411, Singapore*

[3] *Research Institute for Applied Mechanics, Kyushu University, Fukuoka 8168580, Japan*

(Received 21 March 2024; accepted 27 June 2024; published 18 July 2024)

The computation of the second-order mean wave drift loads on a body with thin perforated shells is fundamental and relevant to a wide range of applications in marine engineering, marine aquaculture, offshore renewable energy, etc. In this work, formulations involving a control surface at a distance from the body are proposed to compute drift loads on structures composed of an impermeable hull and a perforated surface accurately and efficiently. Applications of mathematical identities and conservation of fluid momentum are proved to yield identical formulations. Due to the presence of perforated shells, an integral caused by the dissipation through perforated surfaces is included in the formulation. The present formulation cannot only give all six components of the mean wave drift force and moment, but also determine the drift loads on each individual body of a multibody system. The developed formulations are applied to a series of structures, including single-body and multibody systems. It is found that the perforated surface integral plays a secondary role in the computation of drift loads. Besides, perforating body surfaces can mitigate the near-trapped wave motion in a multibody system. Compared to a fixed system, the mean wave drift loads can be amplified around the resonance frequencies of body motions. The dissipation through the perforated shell can enhance the damping effect and suppress the excessive motion response, resulting in a reduction in the amplified drift loads.

DOI: 10.1103/PhysRevFluids.9.074802

I. INTRODUCTION

Perforated structures with slots or pores are utilized across a wide range of coastal and offshore applications. They are key components in breakwaters for dissipating wave energy [1,2] and in wave energy devices for harnessing wave power [3–5]. Additionally, they are used in wave absorption in flumes or basins [6,7], motion dampers for marine structures [8–10], and sloshing reduction in liquid tanks [11–13].

Wave interaction with perforated structures can be modeled using various approaches. High-fidelity computational fluid dynamics (CFD) methods can accurately capture the complex flow features through perforated surfaces, though they require refined meshes and result in high computational costs [14–17]. Alternatively, potential flow theory is widely used, assuming the perforated geometry is thin with fine pores. This approach does not explicitly model the flow through the slots or pores but employs a linear or quadratic relationship between pressure drop and cross-flow velocity. Linear resistance laws have been derived using Darcy's law [18] or a convection-neglected

*Contact author: liang_hui@tcoms.sg

Euler equation model [19]. Linear resistance laws have been widely applied to evaluate breakwaters' performance through analytical methods or boundary element models.

In oscillatory flows, the normal velocity of the fluid across a perforated surface can lead to energy loss due to flow separation at the edges of the openings. Consequently, the pressure drop across the perforated surface can be expressed as a combination of a quadratic drag term and an inertial term due to flow acceleration through the openings [8,9]. This quadratic pressure drop has been explicitly considered in numerous studies to predict the added mass and damping for perforated stabilizers or plates undergoing forced motions [9,20,21] and to compute wave forces on thin perforated sheets [22]. A numerical model based on a boundary element method was established by Mackay *et al.* [23] to compute wave forces on structures with perforated elements, considering both linear and quadratic pressure-velocity relationships. Additionally, reciprocal hydrodynamic identities for quadratic pressure discharge conditions were derived. Liang *et al.* [24] also considered hydrodynamic loads on perforated elastic plates subject to a quadratic pressure drop condition.

For the design of station-keeping systems for floating bodies, the nonlinear slow-drift motion is a critical issue. It is generally understood that the second-order difference-frequency wave force is the primary source of excitation [25]. Reliable semianalytical solutions and numerical models for the second-order wave force in bichromatic waves have been developed [26–28]. To achieve a complete resolution of the difference-frequency wave force, second-order wave theory is necessary. Due to the nonlinearity and intrinsic complexity of boundary conditions over the infinite free surface and the moving body surface, complex formulations and intensive computational efforts are required for complete solutions. Therefore, different approximations have been proposed [29–32]. One of the widely used approximations is Newman's approximation [29], in which the difference-frequency wave force is expanded into a Taylor's series concerning the frequency difference, and only the zero-order component is retained. Consequently, the exact difference-frequency wave force is approximated by the mean wave drift force on structures in regular waves.

All of the approximations above show the importance of the mean wave drift force to the low-frequency behavior of a floating body. To date, the mean wave drift force on impermeable bodies has been extensively studied. This study focuses on wave drift loads on structures with perforated surfaces. The wave force on perforated shells arises from the pressure difference between their outer and inner surfaces. Researchers have computed the mean wave drift force on a perforated body using either a far-field formulation or a near-field formulation [23,33–37]. The far-field formulation, which applies the momentum theorem to the fluid domain, is limited to providing only mean wave drift surge/sway forces and yaw moments around the vertical axis. Whereas the near-field formulation is based on direct pressure integration over the body surface. For complex geometries, singularities in the velocity field around sharp corners of the hull can lead to poor convergence when integrating the quadratic pressure over the body surface [38,39]. Therefore, efforts have been made to improve computational accuracy, leading to formulations for evaluating the mean wave drift force on impermeable bodies [38–40].

Encouraged by the advancements for impermeable bodies, this study develops a formulation to compute mean wave drift forces and moments on structures with perforated shells. This formulation is derived either by transforming the conventional direct pressure integration method to one involving a control surface at a distance from the body or by applying the conservation of fluid momentum in a control volume enclosing the body. The inclusion of perforated shells introduces a dissipation term due to the flow through the perforations. This new formulation can determine all components of the mean wave drift forces and moments, making it more comprehensive than the far-field formulation. Moreover, unlike the traditional near-field formulation, this approach does not require the fluid velocity over the impermeable hull surface, which is typically singular at sharp corners, thereby improving accuracy. To demonstrate the advantages of the developed formulations, numerical examples for a variety of structures are presented following an elaborate derivation.

The layout of the paper is as follows. In Sec. II, we present the basic assumptions and the boundary value problem. Section III sets forth an elaborate derivation of the formulation for determining the mean wave drift loads on bodies with perforated shells in the time domain, followed by the

corresponding formulations in the frequency domain presented in Sec. IV. Numerical examples for single/multiple perforated cylinder and a compound cylinder with a perforated shell are exhibited in Sec. V. Finally, concluding remarks are presented in Sec. VI. Key procedures for deriving analytical solutions to numerical examples are detailed in Appendixes A and B.

II. MATHEMATICAL MODEL

The interaction of water waves with structures containing thin perforated shells is concerned in this study. The structure is assumed to consist of a single impermeable body and a perforated surface enclosing a volume of water connected to the body. A reference system in Cartesian coordinates is defined with the oxy plane ($z = 0$) coinciding with the undisturbed free surface and z axis orienting vertically upward. The perforated part of the structure is assumed to be thin with fine pores and is treated as a homogeneous surface. The flow through the perforated shell is approximately modeled as a pressure drop dependent on the fluid velocity normal to the perforated surface, as in Refs. [8,18,19]. Away from the perforated surface, the fluid is assumed to be inviscid and incompressible, and its motion is irrotational. Under these assumptions of a perfect fluid, a velocity potential Φ satisfying the Laplace equation can be used to describe the fluid motion

$$\nabla^2\Phi(x, y, z, t) = 0. \tag{1}$$

Besides the Laplace equation, appropriate boundary conditions on the mean free surface at $z = 0$ and the seabed at $z = -h$ are also required. The linear free-surface boundary condition is

$$\frac{\partial^2\Phi}{\partial t^2} + g\frac{\partial\Phi}{\partial z} = 0, \quad \text{on} \quad z = 0, \tag{2}$$

where g is the acceleration due to gravity, and t denotes time. The seabed condition is written as

$$\frac{\partial\Phi}{\partial z} = 0, \quad \text{on} \quad z = -h. \tag{3}$$

We define S_b as the impermeable wetted body surface, and S_w^+ and S_w^- as the outer and inner sides of the perforated surface, respectively. On S_b, the normal vector is defined as positive, pointing out of the fluid domain. In the meantime, the normal vectors on S_w^+ and S_w^- are defined as pointing into the interior and exterior regions, respectively. On the impermeable surface S_b, the body boundary condition is

$$\frac{\partial\Phi}{\partial n} = \dot{\mathbf{X}} \cdot \mathbf{n}, \quad \text{on } S_b, \tag{4}$$

where the overdot means the derivative with respect to time t, and $\mathbf{X} = (X_1, X_2, X_3)^T$ denotes the first-order displacements due to the translational and rotational motions of the structure, which are written as

$$\mathbf{X} = \boldsymbol{\Xi} + \mathbf{A} \times \hat{\mathbf{r}}, \quad \text{with } \hat{\mathbf{r}} = \mathbf{x} - \mathbf{x}_o, \tag{5}$$

where $\boldsymbol{\Xi} = (\Xi_1, \Xi_2, \Xi_3)^T$ denotes the translational motion vector, $\mathbf{A} = (A_1, A_2, A_3)^T$ is the rotational motion vector, and $\mathbf{x}_o$ is the rotational center.

On the perforated surface, the normal velocity components on both sides are continuous, whereas there exists a pressure difference across the perforated surface. It is assumed that the shells are thin and of fine pores, and we are concerned with the actions of incident waves of small steepness. The pressure drop through the perforated shell can be assumed linearly proportional to the normal velocity. The linear pressure discharge condition on the perforated surface is written as [18,41]

$$-\frac{\partial(\Phi^+ - \Phi^-)}{\partial t} = \pm\frac{\mu}{\rho\gamma}W_n, \quad \text{on } S_w^{\pm}, \tag{6}$$

where ρ is the fluid density; Φ^+ and Φ^- denote the velocity potential on the outer and inner sides of the perforated surface, respectively; μ is the dynamic fluid viscosity; γ is a coefficient with a dimension of length ranging from 0 to $+\infty$ with $\gamma = 0$ and $\gamma = +\infty$ corresponding to impermeable and transparent scenarios, respectively; W_n is the relative fluid velocity in the direction normal to the boundary surface. W_n can be written as

$$W_n = \frac{\partial \Phi}{\partial n} - \{\dot{\boldsymbol{\Xi}} \cdot \mathbf{n} + \dot{\mathbf{A}} \cdot [(\mathbf{x} - \mathbf{x}_o) \times \mathbf{n}]\}. \tag{7}$$

III. SECOND-ORDER MEAN WAVE DRIFT LOADS ON STRUCTURES WITH PERFORATED SHELLS

Once the boundary-value problem described in Sec. II is solved, the first-order physical quantities are obtained. The linear wave loads can be determined via direct integration of the first-order pressure. The second-order wave forces and moments $(\mathbf{F}_2, \mathbf{M}_2)$ can be decomposed into

$$(\mathbf{F}_2, \mathbf{M}_2) = (\mathbf{F}_{21}, \mathbf{M}_{21}) + (\mathbf{F}_{22}, \mathbf{M}_{22}), \tag{8}$$

where $(\mathbf{F}_{21}, \mathbf{M}_{21})$ is due to the quadratic products of the first-order quantities, and $(\mathbf{F}_{22}, \mathbf{M}_{22})$ is contributed by the second-order velocity potential, which is determined by the second-order boundary-value problem. The mean drift wave force, which we are concerned with here, is the time-independent components of $(\mathbf{F}_{21}, \mathbf{M}_{21})$, and $(\mathbf{F}_{21}, \mathbf{M}_{21})$ can be further decomposed into

$$(\mathbf{F}_{21}, \mathbf{M}_{21}) = (\mathbf{F}_q, \mathbf{M}_q) + (\mathbf{F}_S, \mathbf{M}_S), \tag{9}$$

where $(\mathbf{F}_q, \mathbf{M}_q)$ are associated with the dynamic pressure integration over the mean position of the hull surface and along the water line, and $(\mathbf{F}_S, \mathbf{M}_S)$ are the second-order variation of the hydrostatic wave force and moment due to the first-order body motions [42], which give only nonzero values for the wave forces in the vertical direction and moments around the horizontal axes. As discussed in Ref. [42], $(\mathbf{F}_S, \mathbf{M}_S)$ depend on the hull geometry and body motions, and thus can be computed easily. In the following context, we focus on the computation of terms $(\mathbf{F}_q, \mathbf{M}_q)$.

The mean wave drift force on the perforated shell is due to the pressure difference on its outer and inner surfaces [33,34]. As a result, for structures that are wall-sided at the waterline and contain perforated surfaces, $(\mathbf{F}_q, \mathbf{M}_q)$ can be expressed as

$$\mathbf{F}_q = -\rho \iint_{S_b \cup S_w^{\pm}} \left[\left(\frac{1}{2} \nabla \Phi \cdot \nabla \Phi + \mathbf{X} \cdot \nabla \frac{\partial \Phi}{\partial t} \right) \mathbf{n} + (\mathbf{A} \times \mathbf{n}) \frac{\partial \Phi}{\partial t} \right] ds + \frac{\rho g}{2} \oint_{\Gamma_b \cup \Gamma_w^{\pm}} [\zeta(\zeta - 2X_3)\mathbf{n}] dl, \tag{10a}$$

$$\mathbf{M}_q = -\rho \iint_{S_b \cup S_w^{\pm}} \left[\left(\frac{1}{2} \nabla \Phi \cdot \nabla \Phi + \mathbf{X} \cdot \nabla \frac{\partial \Phi}{\partial t} \right) \hat{\mathbf{n}} + (\boldsymbol{\Xi} \times \mathbf{n} + \mathbf{A} \times \hat{\mathbf{n}}) \frac{\partial \Phi}{\partial t} \right] ds + \frac{\rho g}{2} \oint_{\Gamma_b \cup \Gamma_w^{\pm}} [\zeta(\zeta - 2X_3)\hat{\mathbf{n}}] dl, \tag{10b}$$

where Γ_b and $\Gamma_w^{\pm}$ are the intersections of S_b and $S_w^{\pm}$ with $z = 0$, respectively, $\hat{\mathbf{n}} = \hat{\mathbf{r}} \times \mathbf{n}$, and ζ denotes the first-order free-surface elevation determined by the dynamic free-surface boundary condition,

$$\zeta = -\frac{1}{g} \frac{\partial \Phi}{\partial t}\bigg|_{z=0}. \tag{11}$$

In addition, in Eq. (10) and subsequent equations, $\iint_{S_w^{\pm}}$ and $\oint_{\Gamma_w^{\pm}}$ mean $\iint_{S_w^-} - \iint_{S_w^+}$ and $\oint_{\Gamma_w^-} - \oint_{\Gamma_w^+}$, respectively.

Integration of the square of fluid velocity is involved in Eq. (10). For structures having a complex geometry, the gradient of velocity potential is singular at sharp corners. Taking a truncated cylinder as an example, the gradient of the perturbed potential at the edge has a minus cubic-root singularity [43]. The singularity problem is more pronounced when the body experiences large motions. As discussed in Refs. [39,44,45], singularities of the fluid velocity components near a sharp corner is challenging to obtain converged computational results of the mean wave drift force. All in all, even though Eq. (10) is easy to be implemented, it is difficult to achieve converged results for structures with a sharp variation in geometry.

A. Application of Gauss' and Stokes' theorems

In this subsection, efforts are made to recast Eq. (10) by means of Gauss' and Stokes' theorems. By applying Stokes' theorem over the body surface, the following expressions can be obtained [38]:

$$\iint_{S_b\cup S_w^{\pm}}\left[\left(\mathbf{X}\cdot\nabla\frac{\partial\Phi}{\partial t}\right)\mathbf{n}-(\mathbf{X}\cdot\mathbf{n})\nabla\frac{\partial\Phi}{\partial t}+(\mathbf{A}\times\mathbf{n})\frac{\partial\Phi}{\partial t}\right]ds=-\oint_{\Gamma_b\cup\Gamma_w^{\pm}}\frac{\partial\Phi}{\partial t}(\boldsymbol{\tau}\times\mathbf{X})dl, \tag{12a}$$

$$\iint_{S_b\cup S_w^{\pm}}\left[\left(\mathbf{X}\cdot\nabla\frac{\partial\Phi}{\partial t}\right)\hat{\mathbf{n}}+(\boldsymbol{\Xi}\times\mathbf{n}+\mathbf{A}\times\hat{\mathbf{n}})\frac{\partial\Phi}{\partial t}-\left(\hat{\mathbf{r}}\times\nabla\frac{\partial\Phi}{\partial t}\right)(\mathbf{X}\cdot\mathbf{n})\right]ds$$
$$=-\oint_{\Gamma_b\cup\Gamma_w^{\pm}}\frac{\partial\Phi}{\partial t}[\hat{\mathbf{r}}\times(\boldsymbol{\tau}\times\mathbf{X})]dl, \tag{12b}$$

where $\boldsymbol{\tau}$ is the tangent vector along the waterline. For structures that intersect the mean free surface vertically, the following relationship holds:

$$\boldsymbol{\tau}\times\mathbf{n}=\mathbf{k},\qquad\text{on }\Gamma_b\text{ and }\Gamma_w^{\pm}, \tag{13}$$

where $\mathbf{k}$ is the unit vector along the positive z axis.

We further consider a control volume Ω_c bounded by the mean wetted body surface as well as S_c and S_f, respectively. S_c represents a fictitious (control) surface surrounding the body, intersecting the mean free surface vertically. S_f is the mean free surface within the control volume. The normal vector on S_c points to the far-field region, whereas that on S_f is oriented upward.

Applying Gauss' theorem in the control volume gives rise to [46]

$$\iint_{S_b\cup S_w^{\pm}\cup S_c\cup S_f}[(\nabla\Phi\cdot\nabla\Phi)\mathbf{n}]ds=2\iint_{S_b\cup S_w^{\pm}\cup S_c\cup S_f}\left(\frac{\partial\Phi}{\partial n}\nabla\Phi\right)ds, \tag{14a}$$

$$\iint_{S_b\cup S_w^{\pm}\cup S_c\cup S_f}[(\nabla\Phi\cdot\nabla\Phi)\hat{\mathbf{n}}]ds=2\iint_{S_b\cup S_w^{\pm}\cup S_c\cup S_f}\left[\frac{\partial\Phi}{\partial n}(\hat{\mathbf{r}}\times\nabla\Phi)\right]ds. \tag{14b}$$

By making use of Eqs. (12) and (14), the mean wave drift force and moment given by Eqs. (10a) and (10b) are rewritten as

$$\mathbf{F}_q=-\rho\iint_{S_b}\frac{\partial}{\partial t}[(\mathbf{X}\cdot\mathbf{n})\nabla\Phi]ds-\rho\iint_{S_w^{\pm}}\left[\frac{\partial\Phi}{\partial n}\nabla\Phi+(\mathbf{X}\cdot\mathbf{n})\nabla\frac{\partial\Phi}{\partial t}\right]ds$$
$$-\rho\iint_{S_c\cup S_f}\left[\frac{\partial\Phi}{\partial n}\nabla\Phi-\frac{1}{2}(\nabla\Phi\cdot\nabla\Phi)\mathbf{n}\right]ds+\frac{\rho g}{2}\oint_{\Gamma_b\cup\Gamma_w^{\pm}}[\zeta^2\mathbf{n}-2\zeta(\mathbf{X}\cdot\mathbf{n})\mathbf{k}]dl, \tag{15a}$$

$$\mathbf{M}_q=-\rho\iint_{S_b}\frac{\partial}{\partial t}\{\hat{\mathbf{r}}\times[(\mathbf{X}\cdot\mathbf{n})\nabla\Phi]\}ds-\rho\iint_{S_w^{\pm}}\left\{\hat{\mathbf{r}}\times\left[\frac{\partial\Phi}{\partial n}\nabla\Phi+(\mathbf{X}\cdot\mathbf{n})\nabla\frac{\partial\Phi}{\partial t}\right]\right\}ds$$
$$-\rho\iint_{S_c\cup S_f}\left\{\hat{\mathbf{r}}\times\left[\frac{\partial\Phi}{\partial n}\nabla\Phi-\frac{1}{2}(\nabla\Phi\cdot\nabla\Phi)\mathbf{n}\right]\right\}ds$$
$$+\frac{\rho g}{2}\oint_{\Gamma_b\cup\Gamma_w^{\pm}}\{\hat{\mathbf{r}}\times[\zeta^2\mathbf{n}-2\zeta(\mathbf{X}\cdot\mathbf{n})\mathbf{k}]\}dl. \tag{15b}$$

Application of Green's theorem over S_f yields

$$\iint_{S_f}\left(\frac{\partial\Phi}{\partial t}\bar{\nabla}\frac{\partial\Phi}{\partial t}\right)ds=\frac{1}{2}\oint_{\Gamma_c\cup\Gamma_b\cup\Gamma_w^{\pm}}\left(\frac{\partial\Phi}{\partial t}\frac{\partial\Phi}{\partial t}\mathbf{n}\right)dl, \tag{16a}$$

$$\iint_{S_f}\left[\frac{\partial\Phi}{\partial t}\left(\hat{\mathbf{r}}\times\bar{\nabla}\frac{\partial\Phi}{\partial t}\right)\right]ds=\frac{1}{2}\oint_{\Gamma_c\cup\Gamma_b\cup\Gamma_w^{\pm}}\left(\frac{\partial\Phi}{\partial t}\frac{\partial\Phi}{\partial t}\hat{\mathbf{n}}\right)dl, \tag{16b}$$

where $\bar{\nabla}$ means the gradient with respect to horizontal coordinates and defined as $\bar{\nabla}=\partial/\partial x\mathbf{i}+\partial/\partial y\mathbf{j}$; Γ_c is the intersection of S_c with $z=0$. With the employment of identities (16), Eqs. (15a) and (15b) are further written as

$$\begin{aligned}\mathbf{F}_q=\mathbf{F}_t&-\rho\iint_{S_w^{\pm}}\left[\frac{\partial\Phi}{\partial n}\nabla\Phi+(\mathbf{X}\cdot\mathbf{n})\nabla\frac{\partial\Phi}{\partial t}\right]ds-\rho\iint_{S_c}\left[\frac{\partial\Phi}{\partial n}\nabla\Phi-\frac{1}{2}(\nabla\Phi\cdot\nabla\Phi)\mathbf{n}\right]ds\\&-\rho\iint_{S_f}\left[\left(\frac{\partial\Phi}{\partial z}\frac{\partial\Phi}{\partial z}-\frac{1}{2}\nabla\Phi\cdot\nabla\Phi\right)\mathbf{k}\right]ds-\frac{\rho g}{2}\oint_{\Gamma_c}(\zeta^2\mathbf{n})dl-\rho g\oint_{\Gamma_b\cup\Gamma_w^{\pm}}[\zeta(\mathbf{X}\cdot\mathbf{n})\mathbf{k}]dl,\end{aligned} \tag{17a}$$

$$\begin{aligned}\mathbf{M}_q=\mathbf{M}_t&-\rho\iint_{S_w^{\pm}}\hat{\mathbf{r}}\times\left[\frac{\partial\Phi}{\partial n}\nabla\Phi+(\mathbf{X}\cdot\mathbf{n})\nabla\frac{\partial\Phi}{\partial t}\right]ds-\rho\iint_{S_c}\hat{\mathbf{r}}\times\left[\frac{\partial\Phi}{\partial n}\nabla\Phi-\frac{1}{2}(\nabla\Phi\cdot\nabla\Phi)\mathbf{n}\right]ds\\&-\rho\iint_{S_f}\left[\left(\frac{\partial\Phi}{\partial z}\frac{\partial\Phi}{\partial z}-\frac{1}{2}\nabla\Phi\cdot\nabla\Phi\right)(\hat{\mathbf{r}}\times\mathbf{k})\right]ds\\&-\frac{\rho g}{2}\oint_{\Gamma_c}(\zeta^2\hat{\mathbf{n}})dl-\rho g\oint_{\Gamma_b\cup\Gamma_w^{\pm}}[\zeta(\mathbf{X}\cdot\mathbf{n})(\hat{\mathbf{r}}\times\mathbf{k})]dl,\end{aligned} \tag{17b}$$

where $\mathbf{F}_t$ and $\mathbf{M}_t$ represent the terms that can be grouped as the derivative with respect to time and are given by

$$\mathbf{F}_t=-\rho\iint_{S_b}\frac{\partial}{\partial t}[(\mathbf{X}\cdot\mathbf{n})\nabla\Phi]ds+\frac{\rho}{g}\iint_{S_f}\frac{\partial}{\partial t}\left(\frac{\partial\Phi}{\partial t}\bar{\nabla}\Phi\right)ds, \tag{18a}$$

$$\mathbf{M}_t=-\rho\iint_{S_b}\frac{\partial}{\partial t}\{\hat{\mathbf{r}}\times[(\mathbf{X}\cdot\mathbf{n})\nabla\Phi]\}ds+\frac{\rho}{g}\iint_{S_f}\frac{\partial}{\partial t}\left[\hat{\mathbf{r}}\times\left(\frac{\partial\Phi}{\partial t}\bar{\nabla}\Phi\right)\right]ds. \tag{18b}$$

Equations (17a) and (17b) provide a way to calculate the second-order wave force and moment contributed by the first-order wave field, including both the sum- and difference-frequency components. In addition, the control surface involved in Eqs. (17a) and (17b) can be arbitrary shaped. It can be at a finite distance from the body or at infinity. When the mean wave drift force and moment are concerned, the contribution from Eqs. (18a) and (18b) is nil [38]. Then, the application of Eqs. (17a) and (17b) does not require the computation of fluid velocity components on an impermeable hull surface.

In Eqs. (17a) and (17b), when the perforated part of the structure becomes impermeable, the integrals over $S_w^{\pm}$ can be grouped as $\partial_t[(\mathbf{X}\cdot\mathbf{n})\nabla\Phi]$ and $\partial_t\{\hat{\mathbf{r}}\times\lceil(\mathbf{X}\cdot\mathbf{n})\nabla\Phi\rceil\}$, respectively, and can thus be incorporated into Eqs. (18a) and (18b), which do not contribute to the mean wave drift force and moment.

B. Conservation of fluid momentum

The derivation based on the conservation of fluid momentum is now considered. By using the kinematic transport theorem and Gauss' theorem, the changing rate of the linear momentum of fluid in a control volume can be expressed as [47,48]

$$\frac{d\mathbb{M}}{dt}=-\iint_{S_W^{\pm}\cup S_B\cup S_F\cup S_C}[P\mathbf{n}+\rho gzn_z\mathbf{k}+\rho\mathbf{u}(\mathbf{u}\cdot\mathbf{n}-U_n)]ds, \tag{19}$$

where $\mathbb{M}$ denotes the linear momentum in the control volume; $S_W^{\pm}$ and S_B denote the instantaneous perforated and impermeable wetted body surfaces, S_C and S_F the instantaneous control surface and free surface within the control volume, respectively, $\mathbf{u} = (u_1, u_2, u_3)^T$ the vector of the fluid velocity, and U_n the normal velocity of the boundary surface. On S_B and S_F, the condition that $\mathbf{u} \cdot \mathbf{n} = U_n$ is satisfied. The control surface is fixed, indicating $U_n = 0$ on S_C. Then, we can relate the wave force $\mathbf{F}$ acting on the structure to the time differentiation of fluid momentum in the control volume

$$\mathbf{F} = \iint_{S_W^{\pm} \cup S_B} P\mathbf{n} ds = -\iint_{S_W^{\pm} \cup S_B} (\rho g z n_z \mathbf{k}) ds - \iint_{S_W^{\pm}} \rho \mathbf{u}(\mathbf{u} \cdot \mathbf{n} - U_n) ds - \iint_{S_F \cup S_C} (P\mathbf{n} + \rho g z n_z \mathbf{k}) ds - \iint_{S_C} \rho \mathbf{u}(\mathbf{u} \cdot \mathbf{n}) ds - \frac{d\mathbb{M}}{dt}. \tag{20}$$

On the right-hand side of Eq. (20), the first term contributes to the hydrostatic forces. When the time average is taken and the periodicity invoked, the last term does not contribute to the mean force.

By using Bernoulli's equation and expanding the quantities from S_C to the mean control surface S_c, the quadratic terms of the integral over the control surface are given in the following form:

$$\mathbf{F}_c = -\rho \iint_{S_c} \left[\frac{\partial \Phi}{\partial n} \nabla \Phi - \frac{1}{2} (\nabla \Phi \cdot \nabla \Phi) \mathbf{n} \right] ds - \frac{\rho g}{2} \oint_{\Gamma_c} (\zeta^2 \mathbf{n}) dl. \tag{21}$$

In Eq. (21), the control surface is assumed to be wall-sided near the free surface. On the right-hand side of Eq. (21), the line integral along the mean waterline Γ_c accounts for the momentum flux from $z = 0$ to the instantaneous waterline.

On the free surface, the fluid pressure is equivalent to atmospheric pressure, which is assumed to be zero. The application of Bernoulli's equation to S_F yields

$$-\iint_{S_F} (P\mathbf{n} + \rho g z n_z \mathbf{k}) ds = \mathbf{k} \left\{ \rho \iint_{S_F} \left[\left(\frac{\partial \Phi}{\partial t} + \frac{1}{2} \nabla \Phi \cdot \nabla \Phi \right) n_z \right] ds \right\}. \tag{22}$$

By applying Eq. (22), the quadratic terms of the integral over S_F are expressed as

$$\mathbf{F}_f = \mathbf{k} \left\{ \rho \iint_{S_f} \left(\frac{\partial^2 \Phi}{\partial t \partial z} \zeta + \frac{1}{2} \nabla \Phi \cdot \nabla \Phi \right) ds - \rho g \oint_{\Gamma_b \cup \Gamma_w^{\pm}} [\zeta (\mathbf{X} \cdot \mathbf{n})] dl \right\}, \tag{23}$$

where the first integral is due to the expansion of the velocity potential from the instantaneous position to the mean position, and the last integral is caused by the movement of the waterline and accounts for the vertical momentum flux over the portion of free surface between the instantaneous waterlines and the mean waterlines.

In the meantime, the quadratic terms of the integral over the perforated surface, which is denoted by $\mathbf{F}_w$, can be expressed as

$$\mathbf{F}_w = -\rho \iint_{S_w^{\pm}} (\nabla \Phi W_n) ds. \tag{24}$$

By taking the time average over one period, the second-order mean wave drift force on the system can be expressed as follows:

$$\mathbf{f}^- = -\rho \left\{ \overline{\iint_{S_w^{\pm}} (\nabla \Phi W_n) ds} + \overline{\iint_{S_c} \left[\frac{\partial \Phi}{\partial n} \nabla \Phi - \frac{1}{2} (\nabla \Phi \cdot \nabla \Phi) \mathbf{n} \right] ds} + \frac{g}{2} \overline{\oint_{\Gamma_c} (\zeta^2 \mathbf{n}) dl} \right\} + \rho \mathbf{k} \left\{ \overline{\iint_{S_f} \left(\frac{\partial^2 \Phi}{\partial t \partial z} \zeta + \frac{1}{2} \nabla \Phi \cdot \nabla \Phi \right) ds} - g \overline{\oint_{\Gamma_b \cup \Gamma_w^{\pm}} \zeta (\mathbf{X} \cdot \mathbf{n}) dl} \right\}. \tag{25}$$

Analogous to the analysis of the mean wave drift force, the changing rate of the angular momentum of the fluid in the control volume can be expressed as [48]

$$\frac{d\mathbb{L}}{dt} = -\iint_{S_W^{\pm}\cup S_B\cup S_F\cup S_C} [P(\hat{\mathbf{r}}\times\mathbf{n}) + \rho g z n_z(\hat{\mathbf{r}}\times\mathbf{k}) + \rho(\mathbf{n}\cdot\mathbf{u} - U_n)(\hat{\mathbf{r}}\times\mathbf{u})]ds, \tag{26}$$

where $\mathbb{L}$ is the angular momentum of the fluid in the control volume. Then, we can relate the wave moment $\mathbf{M}$ to the time differentiation of the angular moment

$$\begin{aligned}\mathbf{M} &= \iint_{S_W^{\pm}\cup S_B} P(\hat{\mathbf{r}}\times\mathbf{n})ds \\ &= -\iint_{S_W^{\pm}\cup S_B} [\rho g z n_z(\hat{\mathbf{r}}\times\mathbf{k})]ds - \iint_{S_W^{\pm}} \rho(\mathbf{n}\cdot\mathbf{u} - U_n)(\hat{\mathbf{r}}\times\mathbf{u})ds \\ &\quad - \iint_{S_F\cup S_C} [P(\hat{\mathbf{r}}\times\mathbf{n}) + \rho g z n_z(\hat{\mathbf{r}}\times\mathbf{k})]ds - \iint_{S_C} \rho(\mathbf{n}\cdot\mathbf{u})(\hat{\mathbf{r}}\times\mathbf{u})ds - \frac{d\mathbb{L}}{dt}.\end{aligned} \tag{27}$$

On the right-hand side of Eq. (27), the first term contributes to the hydrostatic moment, and the last term is nil by taking the time average over one period. By using Bernoulli's equation and Taylor's series expansion, the quadratic terms of the integral over the control surface, free surface, and perforated surface, denoted by $\mathbf{M}_c$, $\mathbf{M}_f$, and $\mathbf{M}_w$, respectively, are written as

$$\mathbf{M}_c = -\rho\iint_{S_c}\left\{\hat{\mathbf{r}}\times\left[\frac{\partial\Phi}{\partial n}\nabla\Phi - \frac{1}{2}(\nabla\Phi\cdot\nabla\Phi)\mathbf{n}\right]\right\}ds - \frac{\rho g}{2}\oint_{\Gamma_c}\zeta^2(\hat{\mathbf{r}}\times\mathbf{n})dl, \tag{28a}$$

$$\mathbf{M}_f = \rho\iint_{S_f}\left[\frac{\partial^2\Phi}{\partial t\partial z}\zeta + \frac{1}{2}(\nabla\Phi\cdot\nabla\Phi)\right](\hat{\mathbf{r}}\times\mathbf{k})ds - \rho g\oint_{\Gamma_b\cup\Gamma_w^{\pm}}\zeta(\mathbf{X}\cdot\mathbf{n})(\hat{\mathbf{r}}\times\mathbf{k})dl, \tag{28b}$$

$$\mathbf{M}_w = -\rho\iint_{S_w^{\pm}} W_n(\hat{\mathbf{r}}\times\nabla\Phi)ds. \tag{28c}$$

By taking the time average, the second-order mean wave drift moment on the structure becomes

$$\begin{aligned}\mathbf{m}^- = &-\rho\overline{\iint_{S_w^{\pm}} W_n(\hat{\mathbf{r}}\times\nabla\Phi)ds} - \rho\overline{\iint_{S_c}\left\{\hat{\mathbf{r}}\times\left[\frac{\partial\Phi}{\partial n}\nabla\Phi - \frac{1}{2}(\nabla\Phi\cdot\nabla\Phi)\mathbf{n}\right]\right\}ds} \\ &- \frac{\rho g}{2}\overline{\oint_{\Gamma_c}\zeta^2(\hat{\mathbf{r}}\times\mathbf{n})dl} + \rho\overline{\iint_{S_f}\left(\frac{\partial^2\Phi}{\partial t\partial z}\zeta + \frac{1}{2}(\nabla\Phi\cdot\nabla\Phi)\right)(\hat{\mathbf{r}}\times\mathbf{k})ds} \\ &- \rho g\overline{\oint_{\Gamma_b\cup\Gamma_w^{\pm}}\zeta(\mathbf{X}\cdot\mathbf{n})(\hat{\mathbf{r}}\times\mathbf{k})dl}.\end{aligned} \tag{29}$$

As the following relations hold:

$$\overline{(\mathbf{X}\cdot\mathbf{n})\nabla\frac{\partial\Phi}{\partial t} + \left(\frac{\partial\mathbf{X}}{\partial t}\cdot\mathbf{n}\right)\nabla\Phi} = \overline{\frac{\partial}{\partial t}[(\mathbf{X}\cdot\mathbf{n})\nabla\Phi]} = 0, \tag{30a}$$

$$\overline{\frac{\partial\Phi}{\partial z}\frac{\partial\Phi}{\partial z} + \frac{\partial^2\Phi}{\partial t\partial z}\zeta} = \overline{\frac{\partial}{\partial t}\left(\frac{\partial\Phi}{\partial z}\zeta\right)} = 0, \tag{30b}$$

the time average of Eqs. (17a) and (17b) is consistent with Eqs. (25) and (29), respectively. It indicates that the application of fluid momentum gives rise to identical formulations for mean wave drift force and moment obtained from direct applications of mathematical identities.

IV. REPRESENTATIONS IN THE FREQUENCY DOMAIN

The formulations to determine the mean wave drift loads on structures with perforated shells in the frequency domain are now considered. The incident waves in a time-harmonic steady state with an angular frequency ω and an amplitude A are considered. Physical quantities are expressed as

$$[\Phi(\mathbf{x},t),\zeta(\mathbf{x},t),\mathbf{X}(t),\boldsymbol{\Xi}(t),\mathbf{A}(t)]=\mathrm{Re}\{[\phi(\mathbf{x}),\eta(\mathbf{x}),\boldsymbol{\chi},\boldsymbol{\xi},\boldsymbol{\alpha}]e^{-i\omega t}\},\tag{31}$$

where Re denotes that the real part is taken, and $i=\sqrt{-1}$ is the imaginary unit. By taking the time average of Eqs. (17a) and (17b), we obtain the formulations of mean wave drift force and moment in the frequency domain. The mean wave drift force is written as

$$\mathbf{f}^{-}=\mathbf{f}_{w}^{-}+\mathbf{f}_{c}^{-}+\mathbf{f}_{f}^{-},\tag{32}$$

with $\mathbf{f}_{w}^{-}$, $\mathbf{f}_{c}^{-}$ and $\mathbf{f}_{f}^{-}$ defined as

$$\mathbf{f}_{w}^{-}=\mathrm{Re}\left[-\frac{\rho}{2}\iint_{S_{w}^{\pm}}(w_{n}\nabla\phi^{*})ds\right],\tag{33a}$$

$$\mathbf{f}_{c}^{-}=\mathrm{Re}\left\{-\frac{\rho}{2}\iint_{S_{c}}\left[\frac{\partial\phi}{\partial n}\nabla\phi^{*}-\frac{1}{2}(\nabla\phi\cdot\nabla\phi^{*})\mathbf{n}\right]ds-\frac{\rho g}{4}\oint_{\Gamma_{c}}[(\eta\eta^{*})\mathbf{n}]dl\right\},\tag{33b}$$

$$\mathbf{f}_{f}^{-}=\mathrm{Re}\left\{-\frac{\rho}{2}\iint_{S_{f}}\left[\left(\frac{\partial\phi}{\partial z}\frac{\partial\phi^{*}}{\partial z}-\frac{1}{2}\nabla\phi\cdot\nabla\phi^{*}\right)\mathbf{k}\right]ds-\frac{\rho g}{2}\oint_{\Gamma_{b}\cup\Gamma_{w}^{\pm}}[\eta^{*}(\boldsymbol{\chi}\cdot\mathbf{n})\mathbf{k}]dl\right\},\tag{33c}$$

where the asterisk denotes complex conjugate.

The mean wave drift moment is

$$\mathbf{m}^{-}=\mathbf{m}_{w}^{-}+\mathbf{m}_{c}^{-}+\mathbf{m}_{f}^{-},\tag{34}$$

with $\mathbf{m}_{w}^{-}$, $\mathbf{m}_{c}^{-}$ and $\mathbf{m}_{f}^{-}$ defined as

$$\mathbf{m}_{w}^{-}=\mathrm{Re}\left[-\frac{\rho}{2}\iint_{S_{w}^{\pm}}w_{n}(\hat{\mathbf{r}}\times\nabla\phi^{*})ds\right],\tag{35a}$$

$$\mathbf{m}_{c}^{-}=\mathrm{Re}\left\{-\frac{\rho}{2}\iint_{S_{c}}\left[\frac{\partial\phi}{\partial n}(\hat{\mathbf{r}}\times\nabla\phi^{*})-\frac{1}{2}(\nabla\phi\cdot\nabla\phi^{*})\hat{\mathbf{n}}\right]ds-\frac{\rho g}{4}\oint_{\Gamma_{c}}(\eta\eta^{*})\hat{\mathbf{n}}dl\right\},\tag{35b}$$

$$\mathbf{m}_{f}^{-}=\mathrm{Re}\left[-\frac{\rho}{2}\iint_{S_{f}}\left(\frac{\partial\phi}{\partial z}\frac{\partial\phi^{*}}{\partial z}-\frac{1}{2}\nabla\phi\cdot\nabla\phi^{*}\right)(\hat{\mathbf{r}}\times\mathbf{k})ds-\frac{\rho g}{2}\oint_{\Gamma_{b}\cup\Gamma_{w}^{\pm}}\eta^{*}(\boldsymbol{\chi}\cdot\mathbf{n})(\hat{\mathbf{r}}\times\mathbf{k})dl\right].\tag{35c}$$

In Eqs. (33a) and (35a), w_n is the amplitude of the relative fluid velocity across the perforated surface, and equals

$$w_{n}=\nabla\phi\cdot\mathbf{n}-\{-i\omega[\boldsymbol{\xi}+\boldsymbol{\alpha}\times(\mathbf{x}-\mathbf{x}_{o})]\cdot\mathbf{n}\}.\tag{36}$$

By using the pressure drop condition in Eq. (6), the following condition is satisfied by w_n on the perforated surface [18,41]

$$w_{n}=\begin{cases}i\kappa_{0}G_{0}(\phi^{+}-\phi^{-}), & \text{on } S_{w}^{+};\\ i\kappa_{0}G_{0}(\phi^{-}-\phi^{+}), & \text{on } S_{w}^{-},\end{cases}\tag{37}$$

where $G_0=\omega\rho\gamma/(\kappa_0\mu)$ is normally defined as the porous-effect parameter, κ_0 is the wave number, satisfying the dispersion relation $\omega^2=g\kappa_0\tanh(\kappa_0 h)$, and ϕ^+ and ϕ^- are the complex spatial potentials on S_w^+ and S_w^-, respectively.

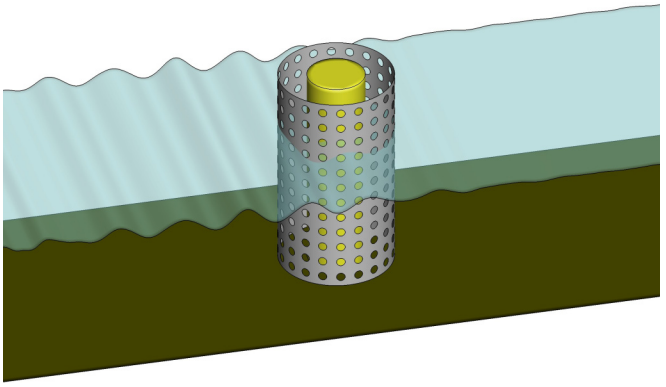

FIG. 1. Sketch of water wave interaction with a bottom-standing concentric perforated cylinder system.

V. RESULTS AND DISCUSSIONS

As a sequel to the derivation of developed formulations in Secs. III and IV, numerical examples are exhibited for a series of structures, including a bottom-standing concentric perforated cylinder system, a square array of bottom-standing perforated cylinders, and a floating concentric perforated cylinder system. Semianalytical solutions to these systems based on eigenfunction expansions are presented in Appendixes A and B, respectively. By a set of experiments for a perforated cylinder in waves, Zhao *et al.* [49] connected the porous-effect parameter G_0 to the opening rate τ of the perforated shell, obtaining

$$G_0 = \frac{1}{2\pi}\frac{\tau^2}{1+1.06\tau}\left(\frac{17.8}{\varepsilon}+143.2\right), \tag{38}$$

in which $\varepsilon = \kappa_0 A$ is the wave steepness. In the subsequent study, Eq. (38) is used to determine the relationship between G_0 and τ with ε being set to 0.10 unless otherwise specified.

A. A bottom-standing concentric perforated cylinder system

We first consider a bottom-standing, surface-piercing, and impermeable cylinder of radius a, surrounded by an exterior cylindrical shell of radius b (see Fig. 1). Both of them are fixed rigidly at the horizontal sea bottom. Such a system can be considered a limiting case of a floating system as the clearance between the system and the seabed approaches zero. Then, the solution to this system can be referred to as those introduced in Appendix A. Figure 2 depicts the frequency response of the horizontal mean wave drift forces on a system of $b/a = 2$ and $h/a = 3$. In addition, the radius of the control surface equals $3a$. In the computation, perforated shells with small opening rates are primarily concerned. The results for porous-effect coefficients $G_0 = 0.2$, 0.6, and 1.0 are displayed in Figs. 2(a), 2(b), and 2(c), respectively. The associated opening rates are $\tau = 6.39\%$, 11.5%, and 15.1%, respectively. The mean wave drift force on a system with an impermeable shell, which amounts to $G_0 = 0.0$, is also presented. The integral over the free surface to the horizontal mean drift force is nil in the present problem. Comparison is made with the far-field method solution, and good agreement has been obtained. Compared to the impermeable shell, a system with a perforated shell experiences larger wave drift loads in long waves corresponding to a small wave number and smaller wave drift loads in short waves at a large wave number. By increasing the porous-effect parameter G_0 associated with the open-area ratio, smaller wave drift forces are generally experienced. In addition, individual contributions from the control surface and perforated surface integrals are also presented. The perforated surface integral gives rise to negative drift forces in general. In all cases, the mean

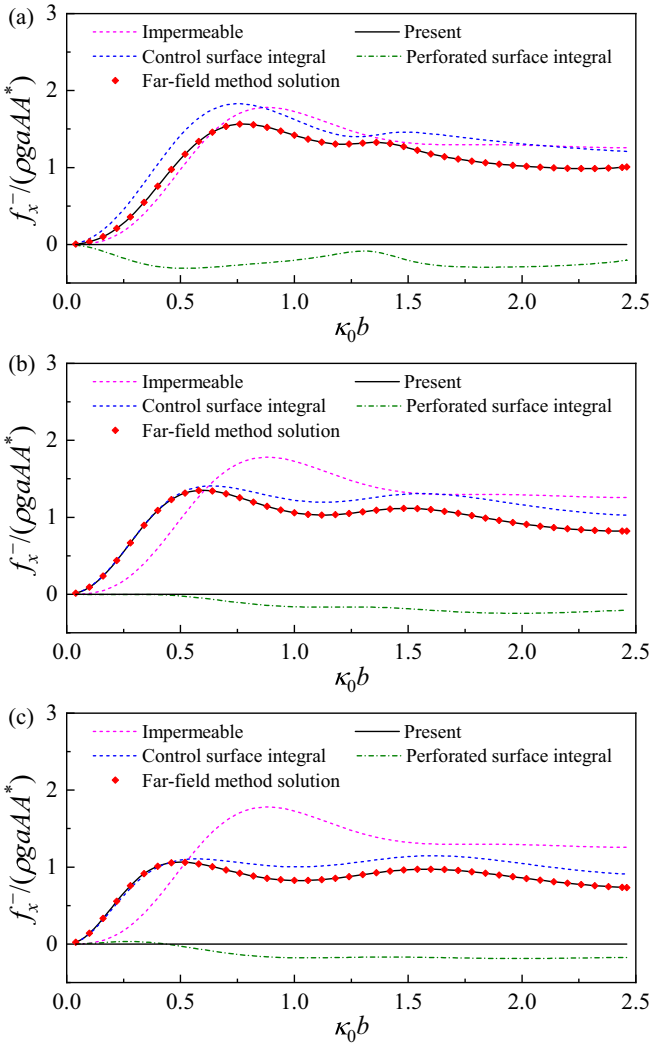

FIG. 2. Horizontal mean wave drift force on a bottom-standing concentric perforated cylinder system when $b/a = 2$ and $h/a = 3$ for $(G_0, \tau) = (0.2, 6.39\%)$, (0.6, 11.5%), and (1.0, 15.1%) as in (a), (b), and (c), respectively. A comparison is made with the far-field method solution by Ref. [35].

wave drift force acting on the system is dominated by the control surface integral, whereas the integral over the perforated surface plays a secondary role.

B. A square array of bottom-standing perforated cylinders

As a sequel to the study of a single body, the focus is now placed on the mean wave drift loads on an array of four identical bottom-standing perforated cylinders, as sketched in Fig. 3. In this case, the far-field formulation can only yield the total drift force on the multibody system, but cannot give rise to that on each individual body. The radius of each cylinder is a, and the center-to-center distance between two cylinders in line with either x axis or y axis is $4a$. The centers of the cylinders are located at $(\pm 2a, \pm 2a)$, and the cylinders are numbered anticlockwise, with cylinder number 1 located in the first quadrant. Solutions based on the near-field formulation and the newly derived

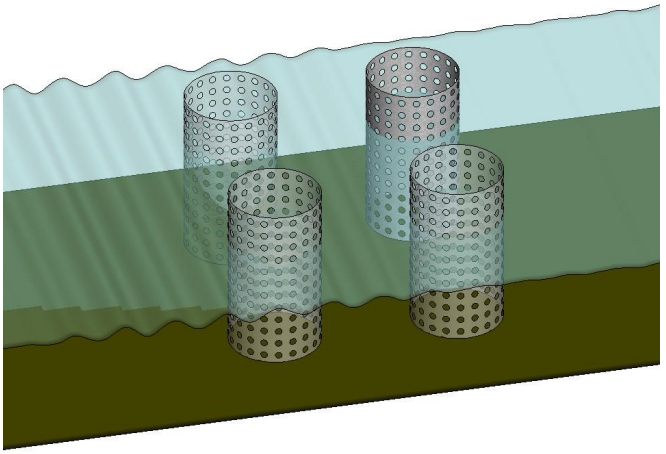

FIG. 3. Sketch of water wave interaction with a square array of bottom-standing perforated cylinders.

formulation are developed in Appendix B. When the newly derived formulation is used, the radius of the control surface surrounding each cylinder equals $1.5a$. Figures 4 and 5 depict the frequency responses of the mean wave drift forces in the direction of wave propagation with $G_0 = 0.1$ and 0.2. The associated opening rates are $\tau = 6.39\%$ and 11.5%, respectively. In the computation, the wave heading is 45° with respect to the positive x axis. Comparison is made between different solutions, and satisfactory agreement has been obtained. Individual contributions from integrals over the control and perforated surfaces are shown, corroborating that the control surface integral is predominant. Besides, the mean wave drift force exerted on an isolated perforated cylinder is also displayed. Strong interference effects in the cylinder array exhibit oscillations with wave numbers in the three subplots. When $G_0 = 0.1$, the maximum mean drift forces on Cylinder 1 that occurred in the range $\kappa_0 a \in (1.5, 2.0)$ are almost twice that on the isolated cylinder. In this range, Cylinder 2 and Cylinder 3 experience negative mean wave drift forces. It can be envisioned that water waves in the region surrounded by cylinders are nearly trapped, resulting in repulsion drift forces on the cylinder array.

The wave trapping in a column array has been demonstrated theoretically and experimentally in previous studies [50–52]. Evans and Porter [50] indicated that the phenomenon of pure wave trapping could occur in a cylinder array when the matrix of coefficients associated with the expansion series has a zero determinant. For the present square array, the wave number where the pure wave trapping occurs is $\kappa_0 a = (1.671, -0.094)$ in the complex space. When the imaginary part of the complex wave number is set to be zero, the wave motion within the region internal to the polygon is weakly damped, leading to a phenomenon of near trapping. Figures 6 and 7 depict the distribution of the free-surface elevation amplitude at $\kappa_0 a = 1.671$ for $\beta = 0°$ and 45°, respectively. In the computation, the porous-effect parameter varies as $G_0 = 0.0$, 0.2, 0.6, and 1.0. The associated opening rates are $\tau = 0.0\%$ (impermeable), 6.39%, 11.5%, and 15.1%. Noticeable wave runups are observed around the cylinders, which is more evident for $\beta = 45°$. Figure 7(a) is characterized by a 2×2 arrangement of peaks and troughs within an impermeable cylinder array. When an apparent peak appears around one cylinder, troughs will simultaneously occur in the local vicinity of the adjacent cylinders, creating a $\begin{pmatrix} + & - \\ - & + \end{pmatrix}$ pattern [50]. If the cylinders become perforated, the wave energy dissipation through the perforated surfaces can reduce the peak wave runup and make a breakdown of the near-trapped wave motion.

The mean wave drift force on the cylinder in the first quadrant is illustrated in Fig. 8 for different wave headings. Around the near-trapping frequency, the positive mean wave drift force with

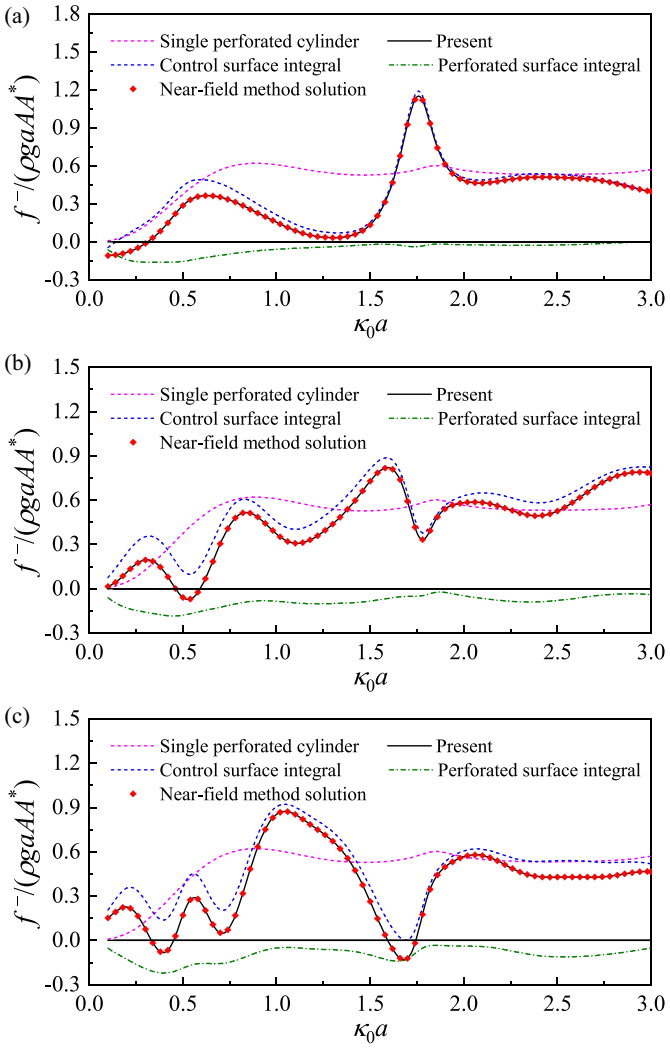

FIG. 4. Mean wave drift forces in the direction of wave propagation for an array of four identical bottom-standing perforated cylinders when $(G_0, \tau) = (0.1, 6.39\%)$ and $\beta = 45^\circ$ of (a) Cylinder 1, (b) Cylinder 2 (or Cylinder 4), and (c) Cylinder 3.

$\beta = 45^\circ$ is enhanced and more apparent than those with other headings. Such enhancement gets reduced by perforating body surfaces, which is consistent with the observation from the wave runup.

C. A floating concentric perforated cylinder system

In the numerical examples presented in Secs. V A and V B, in which bottom-standing perforated cylinders are studied, there is no sharp corner, and therefore, the corresponding singularity does not appear. Here, we consider the wave interaction with a floating concentric perforated cylinder system, as illustrated in Fig. 9, in which the sharp corner singularity matters. In the present example, the floating system consists of a compound cylinder and a perforated sidewall. The compound cylinder has an inner column of radius a and a bottom base of radius $b = 2a$ and height $e = 0.1a$. The perforated shell has the same radius as the bottom base. The draft of the system is $d = 1.3a$, and the water depth is $h = 10a$, as shown in Fig. 10. Solutions based on the far-field formulation and

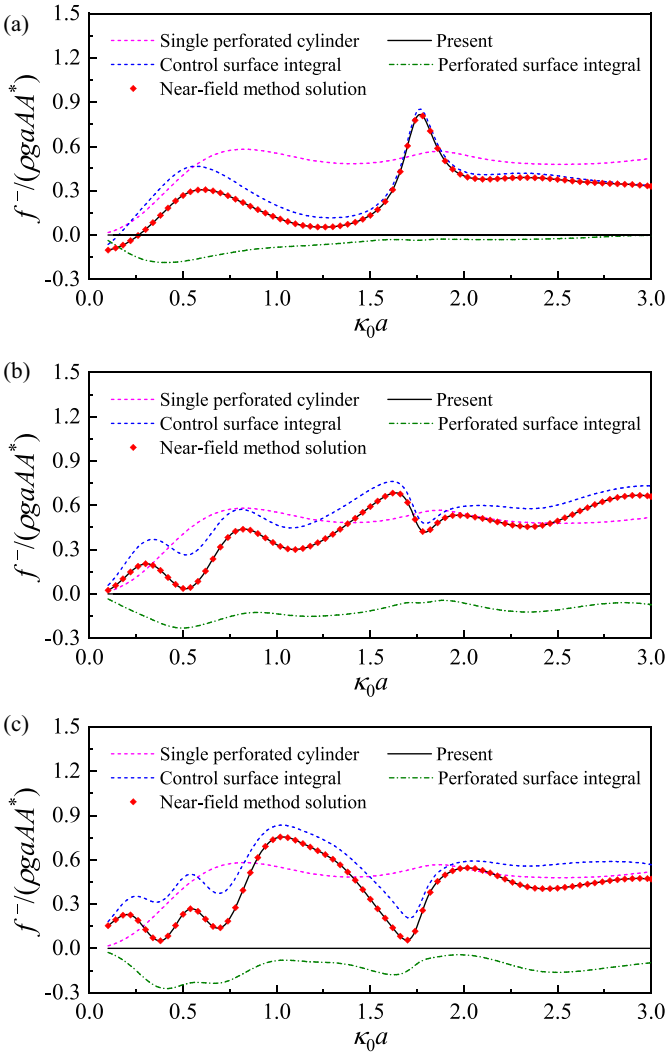

FIG. 5. Mean wave drift forces in the direction of wave propagation for an array of four identical bottom-standing perforated cylinders when when $(G_0, \tau) = (0.2, 11.5\%)$ and $\beta = 45^\circ$ of (a) Cylinder 1, (b) Cylinder 2 (or Cylinder 4), and (c) Cylinder 3.

the newly derived formulation are developed in Appendix A. When the newly derived formulation is used, the radius of the cylindrical control surface is $R_c = 3a$. Numerical results of the body motion and the mean drift wave force are presented. The rotational center is at (0, 0, 0). Other quantities, such as the wave exciting force, added mass, and damping coefficients, have been studied in previous studies [23,36,53], and hence they are not discussed here for brevity.

In the computation, we assume that the mass of the system is evenly distributed over the submerged impermeable part, and the mass of the thin perforated shell is negligible. Figure 11 depicts the surge, heave, and pitch motion amplitude of the system for a series of porous-effect parameters, i.e., $G_0 = 0.0$, 0.05, 0.1, 0.15, and 0.2. The associated opening rates are $\tau = 0.0\%$ (impermeable), 3.02%, 4.42%, 5.48%, and 6.39%. The legend in Fig. 11 is the combination of G_0 and τ, i.e., (G_0, τ). In Fig. 11, the surge or heave motion amplitude is normalized by the incident wave amplitude. However, that for the pitch motion is normalized by the wave steepness parameter $\varepsilon = \kappa_0 A$. The

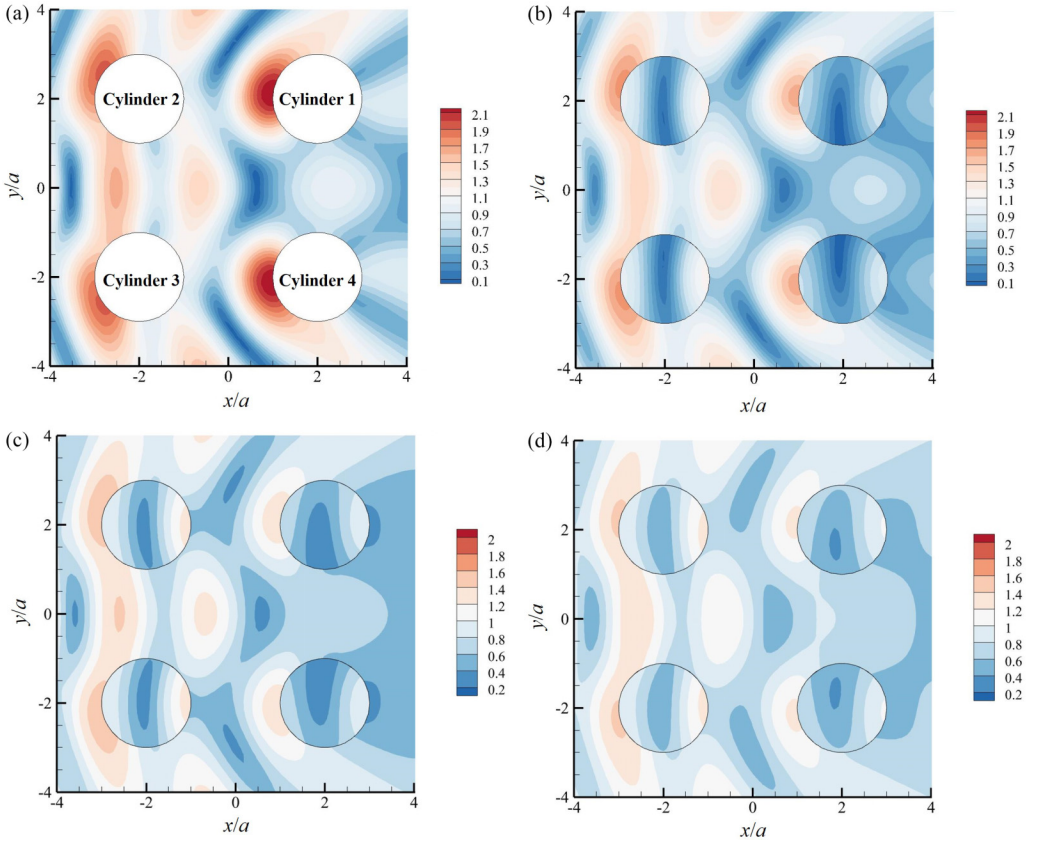

FIG. 6. Distribution of the free-surface elevation amplitude around a square array of bottom-standing cylinders when $\kappa_0 a = 1.671$ and $\beta = 0^\circ$ for impermeable cylinders as in (a) and for perforated cylinders with $(G_0, \tau) = (0.2, 6.39\%)$, $(0.6, 11.5\%)$, and $(1.0, 15.1\%)$ as in (b), (c), and (d), respectively.

system is freely floating in waves, and no external damping or mooring force is applied. Due to the lack of restoring force, the surge motion is significant in long waves. In addition, owing to the small water-plane area of the system, the restoring moment for the pitch motion is low. This leads to a low resonance frequency of the pitch motion, which is around $\kappa_0 a = 0.055$. It should be noted that the apparent low-frequency motion in Figs. 11(a) and 11(c) are based on the assumption that the action of long incident waves is strong. However, in the actual ocean environment, the incident wave energy of long waves remains at a low level. It suggests that the long incident waves are not the main source of the excitation for the low-frequency motion. Noticeable peak motion response can also be found in the wave-frequency region for each motion mode. For structures with perforated elements, the damping for the body motions includes not only conventional wave radiation damping but also a term related to the dissipation through the perforated surface [33]. The latter term can obviously enhance the damping effect. Therefore, as shown in Fig. 11, the peak motion response can be noticeably reduced after the exterior shell becomes perforated.

The heave motion response is then calculated in an expanded range of G_0, in which G_0 varies from 0.5 to $+\infty$. The calculated results are shown in Fig. 12. As G_0 increases, the peak have response amplitude operator (RAO) decreases first, and then increases again. Moreover, the frequency of peak RAO moves gradually to the high-frequency region as G_0 increases. This is related to the added mass caused by the movement of the entrapped fluid between the exterior shell and the interior

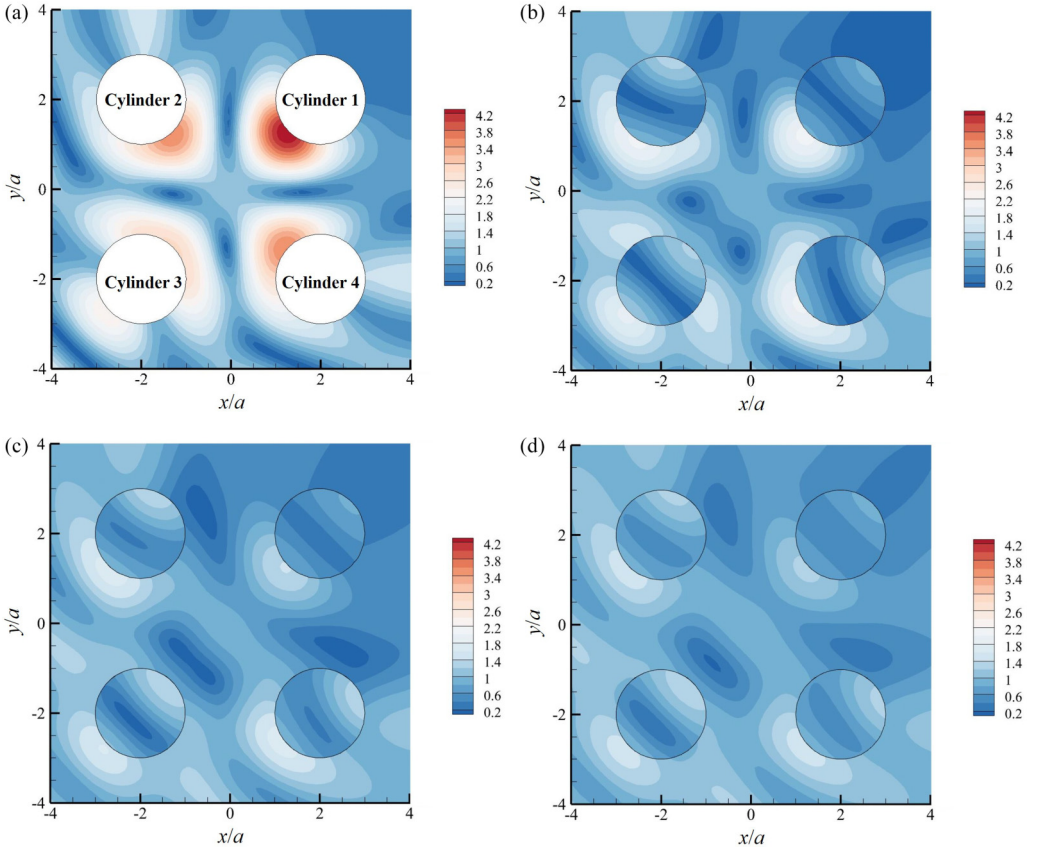

FIG. 7. Distribution of the free-surface elevation amplitude around a square array of bottom-standing cylinders when $\kappa_0 a = 1.671$ and $\beta = 45^\circ$ for impermeable cylinders as in (a) and for perforated cylinders with $(G_0, \tau) = (0.2, 6.39\%)$, (0.6, 11.5%), and (1.0, 15.1%) as in (b), (c), and (d), respectively.

column. In addition, as expected, when the exterior shell is removed, i.e., G_0 tends to $+\infty$, there exist a zero value at the cancellation frequency around $\kappa_0 a = 0.18$.

We then consider the computation of mean wave drift loads on the system. The variation of the present and the near-field solution of the horizontal mean wave drift force at $\kappa_0 a = 0.55$, 0.7, and 0.8 is shown in Table I for different truncated numbers of eigenmodes N. In all the cases, the present solution possesses good convergence characteristics and is consistent with the far-field solution when N is less than 80. Nevertheless, the convergence of the near-field solution versus the increasing number of eigenmodes is much slower than that of the present solution. This is owing to the fact that the integration of the quadratic velocity term over the bottom edge, around which the fluid velocity components are singular, would affect the overall accuracy.

Figure 13 depicts the mean wave drift force and moment on a freely floating concentric perforated cylinder system. The results indicate that the body motion can result in a noticeable effect on the mean wave drift loads. Around the resonance frequencies of the heave and pitch motions, the horizontal mean wave drift force is amplified. In short waves, a series of small peaks can be observed from the horizontal mean force. Similar phenomena have been found for the bottom-standing concentric perforated cylinder systems [35], which is due to that at specific wave frequencies, certain propagation modes of the incident waves can pass through the exterior perforated shell without any dissipation, enhancing the wave impact on the system. The effect of body motions on the vertical mean wave drift wave is also evident. A negative mean force appears around the

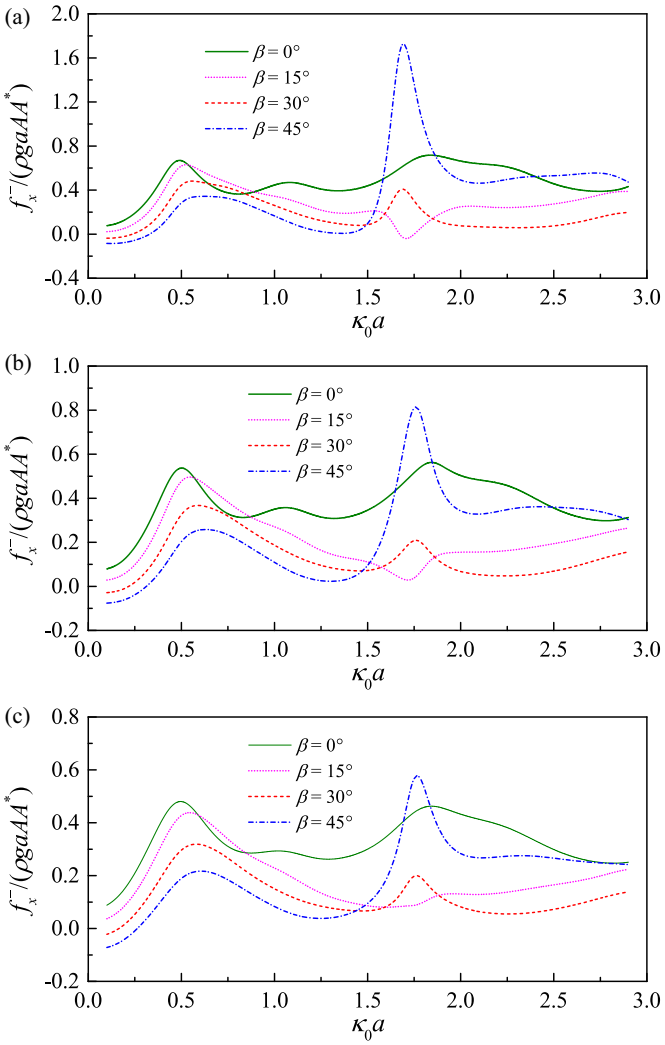

FIG. 8. Mean wave drift force on the cylinder in the first quadrant for a square array of impermeable cylinders as in (a) and perforated cylinders with $(G_0, \tau) = (0.1, 4.42\%)$ and $(0.2, 6.39\%)$ as in (b) and (c), respectively.

resonance frequency of heave motion. The mean wave drift moment exhibits combined features of the horizontal and vertical mean wave drift force. Amplified positive and negative mean wave drift moments are found around the resonance frequencies of the heave and pitch motions. As the dissipation through the perforated shell can enhance the damping and suppress the excessive body motions, the vastly amplified mean wave drift force and moment are noticeably reduced after perforating the exterior shell.

Figures 14 and 15 depict the horizontal and vertical mean wave drift force and its constituent components on a floating concentric cylinder system, either fixed or freely floating in waves. For the horizontal force, the comparison is made with the far-field method solution, and good agreement has been obtained. As shown in Fig. 14, the control surface integral is predominant for the horizontal mean force on either a fixed or a free-floating system. The perforated surface integral generally makes a negative contribution to the horizontal force. For the vertical mean force (see Fig. 15),

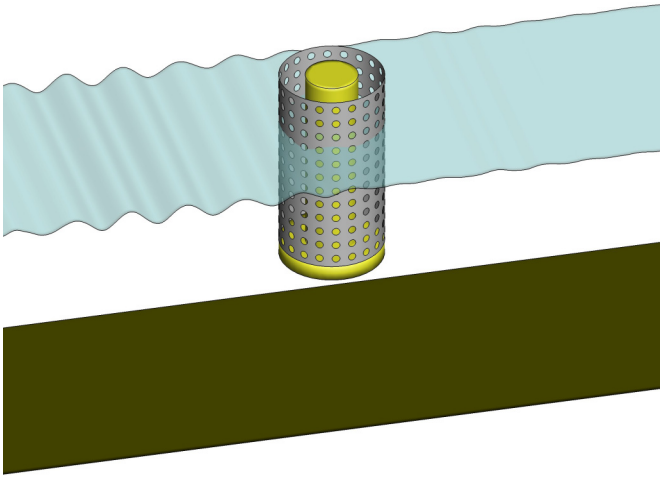

FIG. 9. Sketch of water wave interaction with a freely floating concentric perforated cylinder system.

the perforated surface integral plays a negligible role, and the whole force is dominated by the free surface and the control surface integrals, which are generally out-of-phase. The comparison of the mean wave drift force on a fixed and a free-floating system shows a remarkable difference that appears around the resonance frequencies of the heave and pitch motions, where the radiated waves can significantly disturb the wave field and cause amplified positive mean horizontal force and negative mean vertical force. In short waves, the results of horizontal mean force for fixed and freely floating systems are comparable, while the vertical mean force decays quickly until vanishing.

As the perforated structures can effectively attenuate wave actions and impose less disturbance to water environments, they have been extensively used in near-shore breakwaters for coastal protection. The present research illuminated that perforated structures can also be used as key components for floating bodies. The second-order mean wave drift loads are mainly caused by

TABLE I. Present and near-field solutions of the horizontal mean wave drift force on a freely floating concentric perforated cylinder system ($b/a = 2$, $e/a = 0.1$, $d/a = 1.3$ and $h/a = 10$) for different numbers (N) of eigenmodes. In addition, $(G_0, \tau) = (0.1, 4.42\%)$. The force is normalized by $\rho g a A A^*$. $N = 200$ is used in the far-field solution shown in this table. The asterisk $*$ means that the relative error with respect to the far-field solution is less than 10^{-4}.

	Present solution			Near-field solution		
$N =$ \ $\kappa_0 a =$	0.55	0.7	0.8	0.55	0.7	0.8
10	1.2150	1.3211	1.4777	0.9824	0.9709	1.2248
20	1.2165	1.3280	1.4795	1.0299	1.0317	1.2653
30	1.2160	1.3285	1.4800	1.0790	1.0916	1.3060
40	1.2154	1.3289	1.4802	1.1080	1.1248	1.3283
50	1.2151	1.3291	1.4803	1.1040	1.1226	1.3279
60	1.2149	1.3293	1.4804	1.1118	1.1322	1.3345
70	1.2148	1.3294	*	1.1312	1.1533	1.3481
80	*	*	*	1.1329	1.1560	1.3503
100	*	*	*	1.1426	1.1669	1.3573
150	*	*	*	1.1562	1.1825	1.3671
200	*	*	*	1.1671	1.1944	1.3746
Far-field solution	1.2146	1.3296	1.4806	1.2146	1.3296	1.4806

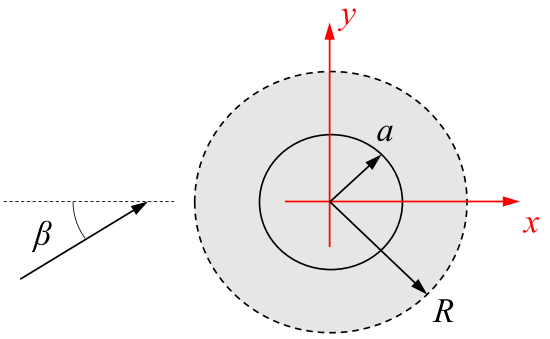

(a) Top view

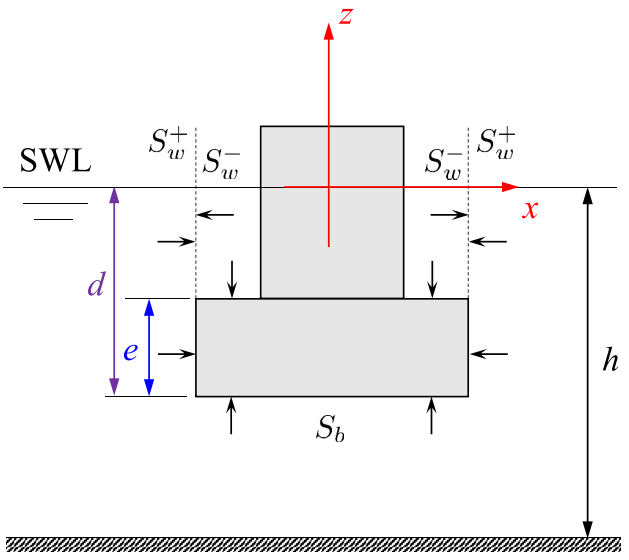

(b) Side view

FIG. 10. Schematic of the geometry and the definition of the coordinate system for a floating concentric perforated cylinder system.

the interaction between the first-order wave fields (including the incident, diffraction and radiation waves) in the wave-frequency region, and are responsible for the low-frequency body motions. The body motions in the wave-frequency and low-frequency regions are coupled closely through the mean wave drift loads. Present results demonstrated that the integration of perforated shells into a floating body could suppress the excessive wave-frequency body motions and in turn reduce the amplified mean wave drift loads. This is beneficial for the mitigation of low-frequency motions. It indicates that applying perforated structures can be a promising way to improve motion stability in a wide frequency range, and can serve the purpose of motion stabilizer for various types of floating structures.

VI. CONCLUSION

In the present study, formulations for the accurate computation of mean wave drift loads on structures with a perforated shell are derived by directly applying Gauss' and Stokes' theorems

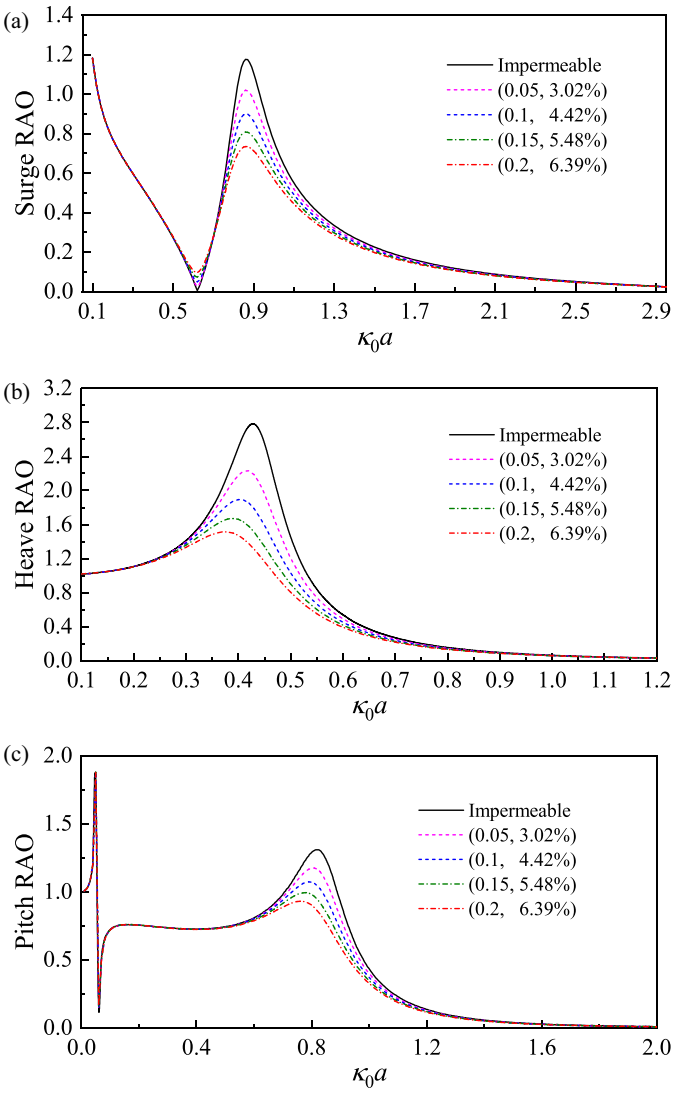

FIG. 11. Normalized motion amplitudes of a floating concentric perforated cylinder system when $b/a = 2$, $e/a = 0.1$, $d/a = 1.3$ and $h/a = 10$ for different combinations of (G_0, τ): (a) surge, (b) heave, and (c) pitch.

or conservation of fluid momentum. The developed formulation involves a control surface surrounding each body. Compared to the far-field formulation, the present formulation can give all six components of the mean wave drift force and moment and can determine the mean wave drift loads on each body of a multibody system. In contrast to the near-field formulation based on direct pressure integration, the computation of fluid velocity components over the impermeable hull surface, which are singular near sharp corners, is no longer required. It is demonstrated that the developed formulations have better convergence than the near-field formulation. The developed formulations are then applied to compute the mean wave drift loads on different types of structures, and good agreement has been obtained by comparing them with benchmark results. Through this study, the following conclusions can be drawn:

(1) The developed formulation transforms the impermeable hull surface integral and part of the perforated surface integral to a control surface at a distance from the body. However, there still

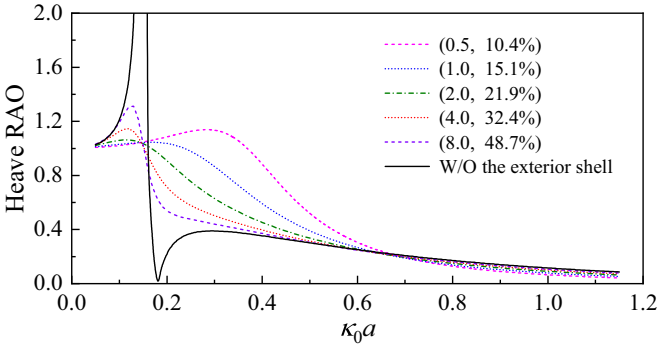

FIG. 12. Normalized heave motion amplitude of a floating concentric perforated cylinder system in an expanded range of G_0 when $b/a = 2$, $e/a = 0.1$, $d/a = 1.3$, and $h/a = 10$.

exists an integral over the perforated surface. Extensive numerical examples demonstrate that the perforated surface integral plays a secondary role, and has limited influence on the overall accuracy.

(2) For a multibody system, the interference effect is non-negligible. When the water waves within the array are nearly trapped, the weather-side body may experience opposing mean wave drift forces. Perforating body surfaces reduce the amplified mean wave drift force on the bodies around the near-trapping frequency and cause a breakdown of the near-trapped wave motion.

(3) For a floating truncated cylinder shielded by a perforated exterior shell, the body motions can impose an appreciable impact on the mean wave drift force. Compared to a fixed system, the mean wave drift loads can be amplified around the body motions' resonance frequencies. The wave energy dissipation through the perforated shell enhances the damping effect and reduces excessive body motion. Therefore, the amplified mean drift wave force or moment is reduced after perforating the exterior shell.

The significance of the present work is threefold. Firstly, the developed formulation enables accurate and efficient computation of mean drift loads on single and multiple bodies with perforated shells. Secondly, the analytical solutions presented here provide benchmark results for the verification of numerical simulations, e.g., the boundary element method. Lastly, this study sheds light on how the application of perforated shells can reduce the mean wave drift loads on floating bodies, which may in turn mitigate the low-frequency motions. This is of practical importance to offshore engineering and marine aquaculture.

ACKNOWLEDGMENTS

P.C. acknowledges support from the National Key Research and Development Program of China [Grant No. 2023YFB4204101], the Joint Funds of the National Natural Science Foundation of China [Grant No. U22A20242], and the Fundamental Research Funds for the Central Universities [Grant No. DUT24ZD104]. Y.L. acknowledges support from Grant-in-Aid for Early-Career Scientists (JSPS) [Grant No. JP22K14430].

APPENDIX A: SOLUTIONS TO THE MEAN WAVE DRIFT FORCE ON A FREELY FLOATING CONCENTRIC PERFORATED CYLINDER SYSTEM

A floating concentric perforated cylinder system is now considered, as illustrated in Figs. 9 and 10. A cylindrical coordinate system is defined with its origin at the center of the interior cylinder and on the still free surface. The z axis orients vertically upwards. The plane incident waves travel along the positive x axis. To facilitate the numerical implementation, a control surface, which consists of

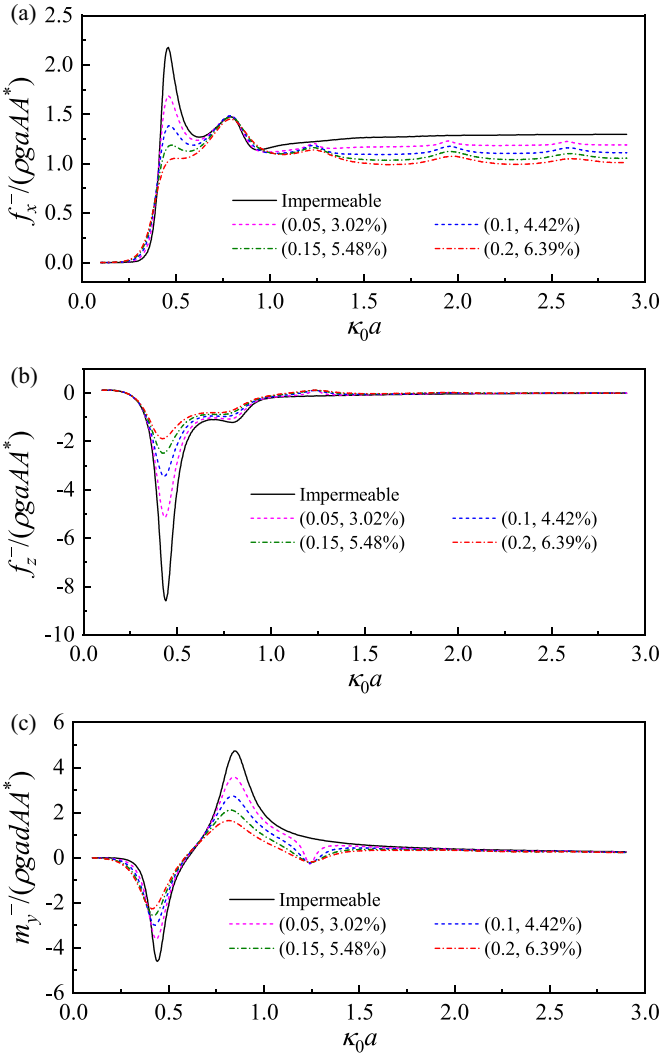

FIG. 13. Mean wave drift wave force and moment on a floating concentric perforated cylinder system when $b/a = 2$, $e/a = 0.1$, $d/a = 1.3$, and $h/a = 10$ for different combinations of (G_0, τ) with the horizontal and vertical force in (a) and (b), and pitch moment in (c).

a cylindrical surface ($r = R_c$ and $-h \leqslant z \leqslant 0$) as well as a circular surface ($r \leqslant R_c$ and $z = -h$), has been used.

The following decomposition of the velocity potential is made:

$$\phi = \phi_I + \phi_D - i\omega \sum_{j=1}^{6} \xi_j \phi_j, \tag{A1}$$

where ϕ_I is the incident velocity potential, and given by

$$\phi_I = -\frac{iAg}{\omega} \frac{\cosh\left[\kappa_0(z+h)\right]}{\cosh\left(\kappa_0 h\right)} e^{i\kappa_0 x}. \tag{A2}$$

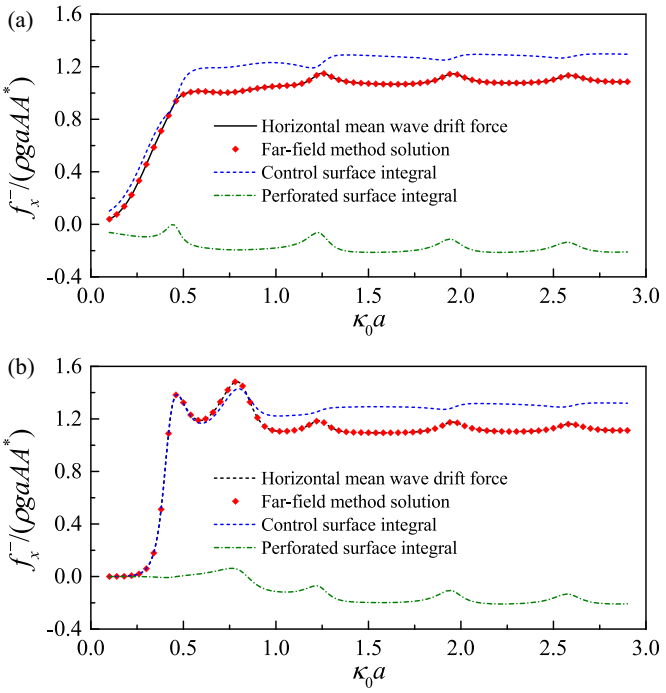

FIG. 14. Horizontal mean wave drift force and its constituent components on a floating concentric perforated cylinder system when $b/a = 2$, $e/a = 0.1$, $d/a = 1.3$, $(G_0, \tau) = (0.1, 4.42\%)$, and $h/a = 10$ of (a) a fixed system, and (b) a freely floating system.

In Eq. (A1), ϕ_D is the diffraction potential due to the presence of the body, and $\phi_j (j = 1, 2, \ldots, 6)$ is the radiation potential due to the body motion in the jth mode. $\hat{\phi}$ is used to denote the summation of the incident and diffraction potentials. That is

$$\hat{\phi} = \phi_I + \phi_D. \tag{A3}$$

The wave diffraction problem is first considered. d_1 is used to denote the height of entrapped fluid within the system, and $S = h - d$ the clearance between the system and seabed. The entire fluid domain is divided into three subdomains: the exterior domain $\Omega_1 (r \geqslant R, -h \leqslant z \leqslant 0)$, the interior domain $\Omega_2 (a \leqslant r \leqslant R, -d_1 \leqslant z \leqslant 0)$, and the lower domain $\Omega_3 (0 \leqslant r \leqslant R, -h \leqslant z \leqslant -d)$. The potential in the nth subdomain is denoted by $\hat{\phi}_n$. By using separation of variables, the velocity potentials valid in each subdomain are expressed as

$$\hat{\phi}_n = -\frac{iAg}{\omega} \sum_{m=0}^{+\infty} \hat{\varphi}_{n,m} \cos m\theta, \quad (n = 1, 2, 3), \tag{A4}$$

where

$$\hat{\varphi}_{1,m}(r, z) = \varepsilon_m i^m \left[J_m(\kappa_0 r) Z_0(\kappa_0 z) + \sum_{j'=0}^{+\infty} \hat{A}_{m,j'} R_{m,j'}(\kappa_{j'} r) Z_{j'}(\kappa_{j'} z) \right], \tag{A5a}$$

$$\hat{\varphi}_{2,m}(r, z) = \varepsilon_m i^m \sum_{k=0}^{+\infty} [\hat{B}_{m,k} P_{m,k}(\mu_k r) + \hat{C}_{m,k} Q_{m,k}(\mu_k r)] U_k(\mu_k z), \tag{A5b}$$

$$\hat{\varphi}_{3,m}(r, z) = \varepsilon_m i^m \sum_{l'=0}^{+\infty} \hat{D}_{m,l'} V_{m,l'}(\lambda_{l'} r) \mathcal{Z}_{l'}(\lambda_{l'} z). \tag{A5c}$$

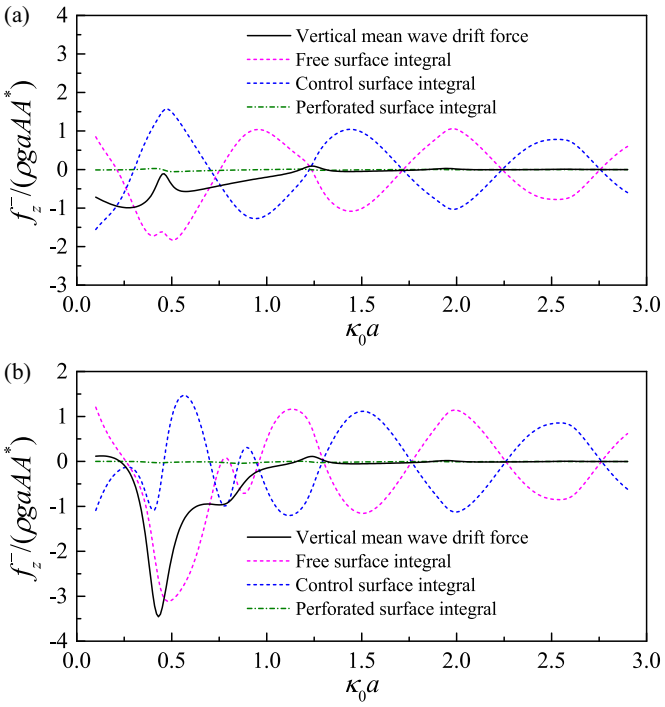

FIG. 15. Vertical mean wave drift force and its constituent components on a floating concentric perforated cylinder system when $b/a = 2$, $e/a = 0.1$, $d/a = 1.3$, $(G_0, \tau) = (0.1, 4.42\%)$, and $h/a = 10$ of (a) a fixed system, and (b) a freely floating system.

In Eq. (A5), $\varepsilon_0 = 1$ and $\varepsilon_m = 2 (m \geqslant 1)$; $\hat{A}_{m,j'}$, $\hat{B}_{m,k}$, $\hat{C}_{m,k}$, and $\hat{D}_{m,l'}$ are the unknown coefficients; $\kappa_{j'} (j' \geqslant 1)$ is the j'th positive real root of $\omega^2 = -g\kappa_{j'} \tan(\kappa_{j'} h)$; μ_0 and ω satisfy the dispersion relation $\omega^2 = g\mu_0 \tanh(\mu_0 d_1)$; $\mu_k (k \geqslant 1)$ is the kth positive real root of $\omega^2 = -g\mu_k \tan(\mu_k d_1)$; the eigenvalues λ_l' are defined as $\lambda_0 = 1$ and $\lambda_{l'} = l'\pi/S (l' \geqslant 1)$; $J_m(\cdot)$ is the mth-order Bessel function of the first kind; $R_{m,j'}(\kappa_{j'} r)$, $P_{m,k}(\mu_k r)$, $Q_{m,k}(\mu_k r)$, and $V_{m,l'}(\lambda_{l'} r)$ are radial functions and defined by

$$R_{m,j'}(\kappa_{j'} r) = \begin{cases} \frac{H_m(\kappa_0 r)}{H_m(\kappa_0 R)}, & j' = 0, \\ \frac{K_m(\kappa_{j'} r)}{K_m(\kappa_{j'} R)}, & j' \geqslant 1, \end{cases} \tag{A6a}$$

$$P_{m,k}(\mu_k r) = \begin{cases} \frac{J_m(\mu_0 r)H_m(\mu_0 a) - J_m(\mu_0 a)H_m(\mu_0 r)}{J_m(\mu_0 R)H_m(\mu_0 a) - J_m(\mu_0 a)H_m(\mu_0 R)}, & k = 0, \\ \frac{I_m(\mu_k r)K_m(\mu_k a) - I_m(\mu_k a)K_m(\mu_k r)}{I_m(\mu_k R)K_m(\mu_k a) - I_m(\mu_k a)K_m(\mu_k R)}, & k \geqslant 1, \end{cases} \tag{A6b}$$

$$Q_{m,k}(\mu_k r) = \begin{cases} \frac{J_m(\mu_0 R)H_m(\mu_0 r) - J_m(\mu_0 r)H_m(\mu_0 R)}{J_m(\mu_0 R)H_m(\mu_0 a) - J_m(\mu_0 a)H_m(\mu_0 R)}, & k = 0, \\ \frac{I_m(\mu_k R)K_m(\mu_k r) - I_m(\mu_k r)K_m(\mu_k R)}{I_m(\mu_k R)K_m(\mu_k a) - I_m(\mu_k a)K_m(\mu_k R)}, & k \geqslant 1, \end{cases} \tag{A6c}$$

$$V_{m,l'}(\lambda_{l'} r) = \begin{cases} \left(\frac{r}{R}\right)^m, & l' = 0, \\ \frac{I_m(\lambda_{l'} r)}{I_m(\lambda_{l'} R)}, & l' \geqslant 1, \end{cases} \tag{A6d}$$

where $H_m(\cdot) = J_m(\cdot) + iY_m(\cdot)$ stands for the Hankel function of the first kind of order m; $I_m(\cdot)$ and $K_m(\cdot)$ are the modified Bessel functions of the first and second kinds of order m, respectively [54], and $Z_{j'}(\kappa_{j'}z)$, $U_k(\mu_k z)$ and $\mathcal{Z}_{l'}(\lambda_{l'}z)$ are orthonormal functions given at the intervals $[-h, 0]$, $[-d_1, 0]$ and $[-h, -d]$, respectively, and defined by

$$Z_{j'}(\kappa_{j'}z) = \begin{cases} \frac{\cosh[\kappa_0(z+h)]}{\cosh(\kappa_0 h)}, & j' = 0, \\ \frac{\cos[\kappa_{j'}(z+h)]}{\cos(\kappa_{j'}h)}, & j' \geqslant 1, \end{cases} \tag{A7a}$$

$$U_k(\mu_k z) = \begin{cases} \frac{\cosh[\mu_0(z+d_1)]}{\cosh(\mu_0 d_1)}, & k = 0, \\ \frac{\cos[\mu_k(z+d_1)]}{\cos(\mu_k d_1)}, & k \geqslant 1, \end{cases} \tag{A7b}$$

$$\mathcal{Z}_{l'}(\lambda_{l'}z) = \begin{cases} \sqrt{2}/2, & l' = 0 \\ \cos[\lambda_{l'}(z+h)], & l' \geqslant 1. \end{cases} \tag{A7c}$$

After truncating the infinite series in Eq. (A5) and accumulating the first $N+1$ terms (from mode 0 to mode N), the above-defined wave diffraction problem can be solved by using the matching conditions and boundary conditions on $r = a$ and $r = R$. More details can refer to Ref. [53], and are not shown here for brevity.

We then proceed to solve the wave radiation problem. Due to the symmetry of the geometry, only the surge, heave, and pitch motions ($j = 1, 3, 5$) can be excited. The radiation potential due to the surge, heave, and pitch motions can be expanded into a Fourier series with respect to θ

$$\phi_{j,n} = \begin{cases} \varphi_n^s \cos\theta, & j = 1, \\ \varphi_n^h, & j = 3, \\ \varphi_n^p \cos\theta, & j = 5, \end{cases} \tag{A8}$$

where the subscript n denotes the potential in the nth subdomain. As the pitch motion owns the combined characteristics of the surge and heave motions, we take the pitch motion as an example to show the solution procedure of wave radiation. The radiation potential due to pitch motion can be expressed as

$$\varphi_1^p(r, z) = \sum_{j'=0}^{+\infty} A_{j'}^p R_{1,j'}(\kappa_{j'}r) Z_{j'}(\kappa_j z); \tag{A9a}$$

$$\varphi_2^p(r, z) = \sum_{k=0}^{+\infty} \left[B_k^p P_{1,k}(\mu_k r) + C_k^p Q_{1,k}(\mu_k r)\right] U_k(\mu_k z) - r\left(z + \frac{1}{v}\right); \tag{A9b}$$

$$\varphi_3^p(r, z) = \sum_{l'=0}^{+\infty} D_{l'}^p V_{1,l'}(\lambda_{l'}r) \mathcal{Z}_{l'}(\lambda_{l'}z) - \frac{r}{2S}\left[(z+h)^2 - \frac{r^2}{4}\right]. \tag{A9c}$$

The last terms on the right-hand side of Eqs. (A9b) and (A9c) are developed to satisfy the inhomogeneous boundary conditions on $z = -d_1$ and $z = -d$, respectively. The velocity potential given in Eq. (A9) describes the flow in the respective region. The unknown coefficients in these expressions can be determined similarly to that in the wave diffraction problem, and hence the details are not presented here for brevity.

As usual, the wave force contributed by incident and diffraction potentials is defined as the wave exciting force $\mathbf{f}_e$ [25]. In the meantime, the radiation force is divided into two parts, which are in phase with the acceleration and velocity of the moving body, respectively. They are normally defined as the added mass a_{jl} and radiation damping b_{jl}. Then, we can have

$$f_{e,j} = i\omega\rho \iint_{S_b \cup S_w^{\pm}} \hat{\phi} n_j ds, \quad (j = 1, 2, \ldots, 6), \tag{A10}$$

and

$$\omega^2\rho\iint_{S_b\cup S_w^{\pm}}\phi_l n_j ds=\omega^2 a_{jl}+i\omega b_{jl},\quad (j,l=1,2,\ldots,6). \tag{A11}$$

When there is no external damping or mooring force applied on the floating system, the translation and rotational motions can be determined by solving the following equation:

$$\sum_{l=1}^{6}[-\omega^2(m_{jl}+a_{jl})-i\omega b_{jl}+c_{jl}]\xi_l=f_{e,j},\quad (j=1,2,\ldots,6), \tag{A12}$$

where m_{jl} and c_{jl} are the coefficients in the mass matrix and restoring force matrix, respectively.

We then turn to the computation of the mean wave drift force. In the nth subdomain, the total potential ϕ_n can be expanded into the following form with respect to θ :

$$\phi_n=\sum_{m=0}^{+\infty}\varphi_{n,m}\cos m\theta,\quad (n=1,2,3), \tag{A13}$$

where

$$\varphi_{n,m}=\begin{cases}\hat{\varphi}_{n,m}-i\omega\xi_3\varphi_n^h, & m=0,\\ \hat{\varphi}_{n,m}-i\omega\left(\xi_1\varphi_n^s+\xi_5\varphi_n^p\right), & m=1,\\ \hat{\varphi}_{n,m}, & m\geqslant 2.\end{cases} \tag{A14}$$

By integrating over $\theta\in[-\pi,\pi]$ and applying orthogonality conditions, different contributions to the horizontal and vertical mean wave drift force on the system are expressed as

$$f_{w,x}^{-}=-\frac{\rho\pi}{4}\,\mathrm{Re}\left\{\int_{-d_1}^{0}\left[i\kappa_0 G_0\sum_{m=0}^{+\infty}\frac{2}{\varepsilon_m}((m+1)\delta_{m+1}^{*}\delta_m-m\delta_m^{*}\delta_{m+1})\right]dz\right\}, \tag{A15a}$$

$$\begin{aligned}f_{c,x}^{-}=\frac{\rho\pi}{4}\,\mathrm{Re}\Bigg\{&\sum_{m=0}^{+\infty}\frac{2}{\varepsilon_m}\int_{-h}^{0}\left(\frac{\partial\varphi_{1,m}}{\partial z}\frac{\partial\varphi_{1,m+1}^{*}}{\partial z}+\frac{m(m+1)}{R_c^2}\varphi_{1,m}\varphi_{1,m+1}^{*}-\frac{\partial\varphi_{1,m}}{\partial r}\frac{\partial\varphi_{1,m+1}^{*}}{\partial r}\right)R_c dz\\&+\sum_{m=0}^{+\infty}\frac{2}{\varepsilon_m}\int_{-h}^{0}\left[m\frac{\varphi_{1,m}}{R_c}\frac{\partial\varphi_{1,m+1}^{*}}{\partial r}-(m+1)\frac{\varphi_{1,m+1}}{R_c}\frac{\partial\varphi_{1,m}^{*}}{\partial r}\right]R_c dz\\&-\sum_{m=0}^{+\infty}\left(\frac{2}{\varepsilon_m}\frac{\omega^2}{g}\varphi_{1,m}\varphi_{1,m+1}^{*}r\right)\Big|_{r=R_c,z=0}\Bigg\},\end{aligned} \tag{A15b}$$

$$f_{f,x}^{-}=0, \tag{A15c}$$

and

$$f_{w,z}^{-}=-\frac{\rho\pi}{2}\,\mathrm{Re}\left\{\int_{-d_1}^{0}\left[i\kappa_0 G_0\sum_{m=0}^{+\infty}\frac{2}{\varepsilon_m}\left(\delta_m\frac{\partial\delta_m^{*}}{\partial z}r\right)\Big|_{r=R}\right]dz\right\}, \tag{A16a}$$

$$\begin{aligned}f_{c,z}^{-}=-\frac{\rho\pi}{4}\,\mathrm{Re}\Bigg\{&\int_{-h}^{0}\left[\sum_{m=0}^{+\infty}\frac{2}{\varepsilon_m}\left(2\frac{\partial\varphi_{1,m}}{\partial r}\frac{\partial\varphi_{1,m}^{*}}{\partial z}r\right)\right]\Bigg|_{r=R_c}dz\\&+\int_{R}^{R_c}\left[\sum_{m=0}^{+\infty}\frac{2}{\varepsilon_m}\left(\frac{\partial\varphi_{1,m}}{\partial r}\frac{\partial\varphi_{1,m}^{*}}{\partial r}+\frac{m^2}{r^2}\varphi_{1,m}\varphi_{1,m}^{*}\right)r\right]\Bigg|_{z=-h}dr\end{aligned}$$

$$+\int_0^R\left[\sum_{m=0}^{+\infty}\frac{2}{\varepsilon_m}\left(\frac{\partial\varphi_{3,m}}{\partial r}\frac{\partial\varphi_{3,m}^*}{\partial r}+\frac{m^2}{r^2}\varphi_{3,m}\varphi_{3,m}^*\right)r\right]\Bigg|_{z=-h}dr\Bigg\}, \tag{A16b}$$

$$f_{f,z}^- = \frac{\rho\pi}{4}\,\mathrm{Re}\left\{\int_R^{R_c}\left[\sum_{m=0}^{+\infty}\frac{2}{\varepsilon_m}\left(\frac{\partial\varphi_{1,m}}{\partial r}\frac{\partial\varphi_{1,m}^*}{\partial r}+\frac{m^2}{r^2}\varphi_{1,m}\varphi_{1,m}^*-\frac{\partial\varphi_{1,m}}{\partial z}\frac{\partial\varphi_{1,m}^*}{\partial z}\right)r\right]\Bigg|_{z=0}dr\right.$$
$$+\int_a^R\left[\sum_{m=0}^{+\infty}\frac{2}{\varepsilon_m}\left(\frac{\partial\varphi_{2,m}}{\partial r}\frac{\partial\varphi_{2,m}^*}{\partial r}+\frac{m^2}{r^2}\varphi_{2,m}\varphi_{2,m}^*-\frac{\partial\varphi_{2,m}}{\partial z}\frac{\partial\varphi_{2,m}^*}{\partial z}\right)r\right]\Bigg|_{z=0}dr$$
$$\left.+2i\omega\xi_1[-(\phi_{2,1}^*r)|_{r=a,z=0}+(\phi_{2,1}^*r)|_{r=R,z=0}-(\phi_{1,1}^*r)|_{r=R,z=0}]\right\}, \tag{A16c}$$

where

$$\delta_m = (\varphi_{1,m}-\varphi_{2,m})|_{r=R}. \tag{A17}$$

The detailed expressions of the mean drift wave moment on the system can be obtained similarly to the wave force, and hence not shown here for brevity.

Besides the newly derived formulation, the mean wave drift force can also be evaluated using the near-field or far-field formulation. Based on Eq. (10a) and the expansion series of the velocity potential, the horizontal mean wave drift force on the system can be expressed as

$$f_x^- = \frac{\rho\pi}{4}\,\mathrm{Re}\left\{\int_{-d_1}^0[\widetilde{u}_2(a,z)+\widetilde{v}_2(a,z)-\widetilde{u}_2(R,z)-\widetilde{v}_2(R,z)]dz\right.$$
$$\left.+\int_{-d}^0[\widetilde{u}_1(R,z)+\widetilde{v}_1(R,z)]dz+[\widetilde{w}_2(a)-\widetilde{w}_2(R)+\widetilde{w}_1(R)]\right\}, \tag{A18}$$

where

$$\widetilde{u}_n(r,z) = \sum_{m=0}^{+\infty}\left[\frac{2}{\varepsilon_m}\left(\frac{\partial\varphi_{n,m}}{\partial r}\frac{\partial\varphi_{n,m+1}^*}{\partial r}+\frac{\partial\varphi_{n,m}}{\partial z}\frac{\partial\varphi_{n,m+1}^*}{\partial z}+\frac{m(m+1)}{r^2}\varphi_{n,m}\varphi_{n,m+1}^*\right)r\right], \tag{A19a}$$

$$\widetilde{v}_n(r,z) = -i\omega\left\{(\xi_1^*+\xi_5^*z)\left(2\frac{\partial\varphi_{n,0}}{\partial r}+\frac{\partial\varphi_{n,2}}{\partial r}+2\frac{\varphi_{n,2}}{r}\right)r\right.$$
$$\left.+\left[2\xi_3^*\frac{\partial\varphi_{n,1}}{\partial z}-\xi_5^*r\left(2\frac{\partial\varphi_{n,0}}{\partial z}+\frac{\partial\varphi_{n,2}}{\partial z}\right)\right]r\right\}, \tag{A19b}$$

$$\widetilde{w}_n(r) = \left\{-\frac{\omega^2}{g}\sum_{m=0}^{+\infty}\left(\frac{2}{\varepsilon_m}\varphi_{n,m}\varphi_{n,m+1}^*r\right)+i\omega[2\xi_3^*\varphi_{n,1}-\xi_5^*r(2\varphi_{n,0}+\varphi_{n,2})]r\right\}\Bigg|_{z=0}. \tag{A19c}$$

In the meantime, when the far-field formulation is used, the horizontal mean wave drift force on the system is

$$f_x^- = \mathrm{Re}\left\{-\frac{\rho}{2}\iint_{S_w^\pm}w_n\frac{\partial\phi^*}{\partial x}ds-\frac{\rho}{2}\iint_{S_\infty}\left[\frac{\partial\phi}{\partial n}\frac{\partial\phi^*}{\partial x}-\frac{1}{2}(\nabla\phi\cdot\nabla\phi^*)n_x\right]ds\right.$$
$$\left.-\frac{\rho g}{4}\oint_{\Gamma_\infty}[(\eta\eta^*)n_x]dl\right\}, \tag{A20}$$

where S_∞ is a cylindrical surface whose radius tends to infinity; Γ_∞ is the intersection of S_∞ at $z=0$. Using asymptotic expressions for Hankel functions, the velocity potential for large r can be

expressed in an asymptotic form

$$\phi(r,z,\theta)=-\frac{iAg}{\omega}\left[e^{i\kappa_0 r\cos\theta}+\sqrt{\frac{2}{\pi\kappa_0 r}}e^{i(\kappa_0 r-\frac{\pi}{4})}\sum_{m=0}^{+\infty}\Pi_m\cos m\theta\right]Z_0(\kappa_0 z), \tag{A21}$$

with

$$\Pi_m=\frac{e^{-\frac{im\pi}{2}}}{H_m(\kappa_0 R)}\left(\varepsilon_m i^m\hat{A}_{m,0}+\frac{\Gamma_m}{-iAg/\omega}\right), \tag{A22a}$$

$$\Gamma_m=\begin{cases}-i\omega\xi_3 A_0^h, & m=0,\\ -i\omega(\xi_1 A_0^s+\xi_5 A_0^p) & m=1,\\ 0, & m\geqslant 2,\end{cases} \tag{A22b}$$

where A_0^s and A_0^h are the expansion coefficients of the propagation mode radiation waves caused by the surge and heave motion, respectively. Inserting Eq. (A21) into Eq. (A20) and applying the stationary phase method, we can obtain

$$\begin{aligned}f_x^- =&-\frac{\rho g A^2}{\kappa_0}\frac{2\kappa_0 h+\sinh 2\kappa_0 h}{2\sinh(2\kappa_0 h)}\operatorname{Re}\left[\sum_{m=0}^{+\infty}2\left(\frac{1}{\varepsilon_m}\Pi_m\Pi_{m+1}^*+\Pi_m\right)\right]\\ &-\frac{\rho\pi}{4}\operatorname{Re}\int_{-d_1}^{0}\left[i\kappa_0 G_0\sum_{m=0}^{+\infty}\frac{2}{\varepsilon_m}((m+1)\delta_{m+1}^*\delta_m-m\delta_m^*\delta_{m+1})\right]dz.\end{aligned} \tag{A23}$$

There are two parameters which influence the accuracy of the computation: the number of eigenmodes N and the number of Fourier modes M. In the present study, $N=100$ is adopted unless otherwise stated. $N=100$ is sufficient to achieve converged results when the derived or the far-field formulation is used. For the sum of the infinite series in Eqs. (A15), (A16), (A19), and (A23), the accuracy is controlled by a truncation tolerance ϵ, which is set as $\epsilon=10^{-6}$, accumulating the first $M+1$ terms (from mode 0 to mode M). M is the smallest value to satisfy

$$\left|\sum_{m=0}^{M+1}-\sum_{m=0}^{M}\right|\Bigg/\left|\sum_{m=0}^{M+1}\right|<\epsilon. \tag{A24}$$

In addition, in the numerical evaluation of the line integrals in Eqs. (A15), (A16), (A18), and (A23), Romberg quadrature was used to control the accuracy.

APPENDIX B: SOLUTIONS TO THE MEAN WAVE DRIFT FORCE ON AN ARRAY OF PERFORATED CYLINDERS

We now focus on the wave interaction with an array of N bottom-standing, surface-piercing, thin-walled perforated cylinders as illustrated in Fig. 16. A global Cartesian coordinate system $oxyz$ is adopted with its origin at the still free surface. The z axis directs vertically upwards. The centers of the perforated cylinders are located at $(x_j,y_j,0)$ $(j=1,2,\ldots,N)$ at the still free surface. Local polar coordinate systems $o_j r_j\theta_j z_j (j=1,2,\ldots,N)$ are defined with their origins located at $(x_j,y_j,0)$ in the global coordinate system. The z_j axis is defined as positive upwards. The wave heading is β with respect to the positive x axis.

The unbounded fluid domain is divided into $N+1$ subdomains: one single exterior region Ω^+ and N interior regions Ω_j^- with $j=1,2,\ldots,N$. The interior regions are defined by $r_j\leqslant a_j (j=1,2,\ldots,N)$ where a_j is the radius of the jth cylinder. The velocity potential in the exterior region is denoted by ϕ^+, while that in the jth interior region is defined by ϕ_j^-. In the jth local polar coordinate

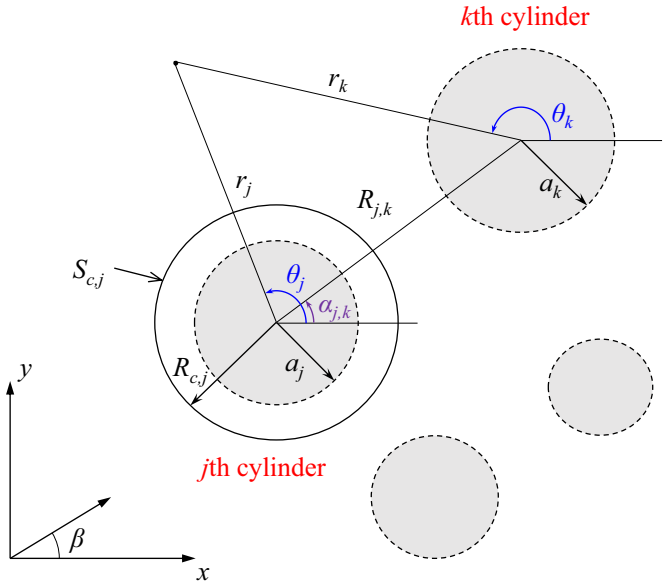

FIG. 16. Plane view of water wave interactions with an array of perforated cylinders and definitions of physical variables.

system, the incident potential ϕ_I can be rewritten as

$$\phi_I(r_j, \theta_j, z_j) = -\frac{iAg}{\omega} I_j^{\beta} \sum_{m=-\infty}^{+\infty} i^m J_m(\kappa_0 r_j) Z_0(\kappa_0 z_j) e^{im(\theta_j - \beta)}, \tag{B1}$$

where I_j^{β} is the phase correction factor associated with the jth cylinder defined by

$$I_j^{\beta} = e^{i\kappa_0(x_j \cos\beta + y_j \sin\beta)}. \tag{B2}$$

The diffraction potential ϕ_D can be expressed as a summation of waves emanating from different cylinders

$$\phi_D = \sum_{j=1}^{N} \sum_{m=-\infty}^{+\infty} A_m^j C_m^j H_m(\kappa_0 r_j) Z_0(\kappa_0 z_j) e^{im\theta_j}, \tag{B3}$$

where A_m^j are unknown coefficients; the factor C_m^j is defined by

$$C_m^j = \frac{J'_m(\kappa_0 a_j)}{H'_m(\kappa_0 a_j)}. \tag{B4}$$

Graf's addition theorem for Bessel functions [54] is then used to express all terms in Eq. (B3) in the same local coordinate system. The velocity potential in the exterior region can then be expressed in

the jth local polar coordinate system as

$$\phi^+(r_j,\theta_j,z_j)=\sum_{m=-\infty}^{+\infty}\psi^+(r_j)Z_0(\kappa_0 z_j)e^{im\theta_j}, \tag{B5}$$

where

$$\psi^+(r_j)=\Lambda_m^j J_m(\kappa_0 r_j)+A_m^j C_m^j H_m(\kappa_0 r_j)+\sum_{\substack{k=1\\k\neq j}}^{N}\sum_{n=-\infty}^{+\infty}A_n^k C_n^k \Delta_{m,n}^{j,k} J_m(\kappa_0 r_j), \tag{B6}$$

with

$$\Lambda_m^j=-\frac{iAg}{\omega}i^m I_j^\beta e^{-im\beta}, \tag{B7}$$

and

$$\Delta_{m,n}^{j,k}=(-1)^m H_{n-m}(\kappa_0 R_{kj})e^{i(n\alpha_{kj}-m\alpha_{jk})}. \tag{B8}$$

In Eq. (B8), R_{kj} is the distance between the centers of the jth and kth cylinders; α_{jk} is the angle between the x axis and the vector from the center of the jth cylinder to that of the kth cylinder. Equation (B8) is valid for $r_j<R_{kj}$, which is true around the wall surface of the cylinders.

According to Ref. [55], the velocity potential in the jth interior region can be expressed as

$$\phi_j^-(r_j,\theta_j,z_j)=\sum_{m=-\infty}^{+\infty}B_m^j J_m(\kappa_0 r_j)Z_0(\kappa_0 z_j)e^{im\theta_j}, \tag{B9}$$

where B_m^j are unknown coefficients. By using the Wronskian relations for Bessel functions, Linton and Evans [56] derived a simple formula for the velocity potential on the cylinders and proposed an improved expression of the mean drift force. Following Linton and Evans [56], the Wronskian relations are used, and the following relationships are yielded:

$$A_m^j\left[1+\frac{2G_0}{\pi\kappa_0 a_j J_m'(\kappa_0 a_j)H_m'(\kappa_0 a_j)}\right]+\sum_{\substack{k=1\\k\neq j}}^{N}\sum_{n=-M}^{+M}A_n^k C_n^k \Delta_{m,n}^{j,k}=-\Lambda_m^j, \tag{B10a}$$

$$B_m^j=-\frac{2G_0}{\pi\kappa_0 a_j}\frac{A_m^j}{J_m'(\kappa_0 a_j)H_m'(\kappa_0 a_j)}, \tag{B10b}$$

where the Fourier modes are truncated from $-M$ to $+M$. The velocity potential in the vicinity of the jth cylinder can be expanded into the following form:

$$\phi^+(r_j,\theta_j,z_j)=\sum_{m=-\infty}^{+\infty}p_{m,j}^+(r_j)Z_0(\kappa_0 z_j)e^{im\theta_j}, \tag{B11a}$$

$$\phi_j^-(r_j,\theta_j,z_j)=\sum_{m=-\infty}^{+\infty}p_{m,j}^-(r_j)Z(\kappa_0 z_j)e^{im\theta_j}, \tag{B11b}$$

where

$$p_{m,j}^+(r_j)=-A_m^j\left[\frac{2G_0}{\pi\kappa_0 a_j}\frac{J_m(\kappa_0 r_j)}{J_m'(\kappa_0 a_j)H_m'(\kappa_0 a_j)}+J_m(\kappa_0 r_j)-C_m^j H_m(\kappa_0 r_j)\right], \tag{B12a}$$

$$p_{m,j}^-(r_j)=-\frac{2A_m^j}{\pi\kappa_0 a_j H_m'(\kappa_0 a_j)}\frac{J_m(\kappa_0 r_j)}{J_m'(\kappa_0 a_j)}G_0. \tag{B12b}$$

Given the first-order velocity potential over the perforated cylinder, the mean wave drift force acting on the jth cylinder can be obtained via direct pressure integration. Then, we can have

$$\begin{Bmatrix} f_{j,x}^{-} \\ f_{j,y}^{-} \end{Bmatrix} = \frac{\rho}{4}\int_{-h}^{0}\int_{0}^{2\pi}\left[(\nabla\phi^{+}\cdot\nabla\phi^{+*} - \nabla\phi_{j}^{-}\cdot\nabla\phi_{j}^{-*})|_{r_j=a_j}\right]\begin{Bmatrix}\cos\theta_j \\ \sin\theta_j\end{Bmatrix}a_j dz_j d\theta_j$$
$$-\frac{\rho}{4}\frac{\omega^2}{g}\int_{0}^{2\pi}\left[(\phi^{+}\phi^{+*} - \phi_{j}^{-}\phi_{j}^{-})|_{r_j=a_j,z_j=0}\right]\begin{Bmatrix}\cos\theta_j \\ \sin\theta_j\end{Bmatrix}a_j d\theta_j. \tag{B13}$$

When $r_j = a_j$, Eq. (B12a) can be reduced to the following form:

$$p_{m,j}^{+}(a_j) = -\frac{2A_m^j}{\pi\kappa_0 a_j H_m'(\kappa_0 a_j)}\left[\frac{J_m(\kappa_0 a_j)}{J_m'(\kappa_0 a_j)}G_0 + i\right], \tag{B14}$$

and Eq. (B13) can be further expressed as

$$\begin{Bmatrix} f_{j,x}^{-} \\ f_{j,y}^{-} \end{Bmatrix} = \frac{\rho\pi a_j}{2}N_0(\kappa_0 h)\cdot\mathrm{Re}\left\{\sum_{m=-\infty}^{+\infty}\begin{Bmatrix}1 \\ -i\end{Bmatrix}\left[\frac{m(m+1)}{a_j^2} - \kappa_0^2\right]\right.$$
$$\left.\cdot\left[p_{m,j}^{+}(a_j)p_{m+1,j}^{+*}(a_j) - p_{m,j}^{-}(a_j)p_{m+1,j}^{-*}(a_j)\right]\right\}, \tag{B15}$$

where $N_0(\kappa_0 h)$ represents the inner products of the vertical eigenfunction $Z_0(\kappa_0 z)$ and defined by

$$N_0(\kappa_0 h) = \int_{-h}^{0} Z_0^2(\kappa_0 z)dz = \frac{1}{\cosh^2(\kappa_0 h)}\frac{h}{2}\left[1 + \frac{\sinh(2\kappa_0 h)}{2\kappa_0 h}\right]. \tag{B16}$$

The computation can also be achieved by using the technique of control surfaces, as discussed in Sec. III. Then, we can have

$$\begin{Bmatrix} f_{j,x}^{-} \\ f_{j,y}^{-} \end{Bmatrix} = \begin{Bmatrix} f_{c,j,x}^{-} \\ f_{c,j,y}^{-} \end{Bmatrix} + \begin{Bmatrix} f_{w,j,x}^{-} \\ f_{w,j,y}^{-} \end{Bmatrix}, \tag{B17}$$

where

$$f_{c,j,x}^{-} = \frac{\rho}{4}\mathrm{Re}\left[\iint_{S_{c,j}}\left(\nabla\phi^{+}\cdot\nabla\phi^{+*}\cos\theta_j - 2\frac{\partial\phi^{+}}{\partial r_j}\frac{\partial\phi^{+*}}{\partial x}\right)ds - \frac{\omega^2}{g}\oint_{\Gamma_{c,j}}\phi^{+}\phi^{+*}\cos\theta_j dl\right], \tag{B18a}$$

$$f_{w,j,x}^{-} = \frac{\rho}{2}\mathrm{Re}\left(\iint_{S_{w,j}^{+}}\frac{\partial\phi^{+}}{\partial r_j}\frac{\partial\phi^{+*}}{\partial x}ds - \iint_{S_{w,j}^{-}}\frac{\partial\phi_j^{-}}{\partial r_j}\frac{\partial\phi_j^{-*}}{\partial x}ds\right). \tag{B18b}$$

$$f_{c,j,y}^{-} = \frac{\rho}{4}\mathrm{Re}\left[\iint_{S_{c,j}}\left(\nabla\phi^{+}\cdot\nabla\phi^{+*}\sin\theta_j - 2\frac{\partial\phi^{+}}{\partial r_j}\frac{\partial\phi^{+*}}{\partial y}\right)ds - \frac{\omega^2}{g}\oint_{\Gamma_{c,j}}\phi^{+}\phi^{+*}\sin\theta_j dl\right], \tag{B19a}$$

$$f_{w,j,y}^{-} = \frac{\rho}{2}\mathrm{Re}\left(\iint_{S_{w,j}^{+}}\frac{\partial\phi^{+}}{\partial r_j}\frac{\partial\phi^{+*}}{\partial y}ds - \iint_{S_{w,j}^{-}}\frac{\partial\phi_j^{-}}{\partial r_j}\frac{\partial\phi_j^{-*}}{\partial y}ds\right). \tag{B19b}$$

In Eqs. (B18) and (B19), $S_{c,j}$ represents a cylindrical surface of radius $R_{c,j}$ surrounding the jth perforated cylinder in the array; $\Gamma_{c,j}$ is the intersection of $S_{c,j}$ with the mean free surface; $S_{w,j}^{+}$ and $S_{w,j}^{-}$ are outer and inner sides of the jth cylinder. As shown in Fig. 16, $S_{c,j}$ extends from the seabed to the free surface and does not intersect with any cylinder in the array. After using Eq. (B11),

Eqs. (B18) and (B19) can be expressed in the following form:

$$\begin{Bmatrix} f^-_{j,c,x} \\ f^-_{j,c,y} \end{Bmatrix} = \frac{\rho\pi}{2} N_0(\kappa_0 h)\,\mathrm{Re}\left(\sum_{m=-\infty}^{+\infty} \mathcal{F}^c_{j,m} \begin{Bmatrix} 1 \\ -i \end{Bmatrix} \right), \tag{B20a}$$

$$\begin{Bmatrix} f^-_{j,w,x} \\ f^-_{j,w,y} \end{Bmatrix} = \frac{\rho\pi}{2} N_0(\kappa_0 h)\,\mathrm{Re}\left(\sum_{m=-\infty}^{+\infty} \mathcal{F}^w_{j,m} \begin{Bmatrix} 1 \\ -i \end{Bmatrix} \right), \tag{B20b}$$

where

$$\begin{aligned} \mathcal{F}^c_{j,m} = {} & \frac{m(m+1)}{R_{c,j}} p^+_{m,j}(R_{c,j}) p^{+*}_{m+1,j}(R_{c,j}) \\ & - \kappa_0^2 R_{c,j} p^+_{m,j}(R_{c,j}) p^{+*}_{m+1,j}(R_{c,j}) - R_{c,j} q^+_{m,j}(R_{c,j}) q^{+*}_{m+1,j}(R_{c,j}) \\ & + m q^{+*}_{m+1,j}(R_{c,j}) p^+_{m,j}(R_{c,j}) - (m+1) q^+_{m,j}(R_{c,j}) p^{+*}_{m+1,j}(R_{c,j}), \end{aligned} \tag{B21a}$$

$$\begin{aligned} \mathcal{F}^w_{j,m} = {} & -m q^{+*}_{m+1,j}(a_j) p^+_{m,j}(a_j) + (m+1) q^+_{m,j}(a_j) p^{+*}_{m+1,j}(a_j) \\ & + m q^{-*}_{m+1,j}(a_j) p^-_{m,j}(a_j) - (m+1) q^-_{m,j}(a_j) p^{-*}_{m+1,j}(a_j). \end{aligned} \tag{B21b}$$

In Eq. (B21), $q^{\pm}_{m,j}$ denotes the differentiation of $p^{\pm}_{m,j}$ with respect to the argument. In Eqs. (B15), (B20a), and (B20b), the sums of the infinite series are controlled by a truncation tolerance ϵ, set as $\epsilon = 10^{-6}$.

[1] Z. Huang, Y. Li, and Y. Liu, Hydraulic performance and wave loadings of perforated/slotted coastal structures: A review, Ocean Eng. **38**, 1031 (2011).

[2] J. Dai, C. M. Wang, T. Utsunomiya, and W. Duan, Review of recent research and developments on floating breakwaters, Ocean Eng. **158**, 132 (2018).

[3] S. Zheng, M. H. Meylan, D. Greaves, and G. Iglesias, Water-wave interaction with submerged porous elastic disks, Phys. Fluids **32**, 047106 (2020).

[4] S. Zheng, M. H. Meylan, G. Zhu, D. Greaves, and G. Iglesias, Hydroelastic interaction between water waves and an array of circular floating porous elastic plates, J. Fluid Mech. **900**, A20 (2020).

[5] H. Liang, S. Zheng, Y. Shao, K. H. Chua, Y. S. Choo, and D. Greaves, Water wave scattering by impermeable and perforated plates, Phys. Fluids **33**, 077111 (2021).

[6] I. H. Cho and M. H. Kim, Wave absorbing system using inclined perforated plates, J. Fluid Mech. **608**, 1 (2008).

[7] W. Sulisz, Numerical modeling of wave absorbers for physical wave tanks, J. Waterw. Port Coastal Ocean Eng. **129**, 5 (2003).

[8] B. Molin, Hydrodynamic modeling of perforated structures, Appl. Ocean Res. **33**, 1 (2011).

[9] S. An and O. M. Faltinsen, An experimental and numerical study of heave added mass and damping of horizontally submerged and perforated rectangular plates, J. Fluids Struct. **39**, 87 (2013).

[10] J. X. Li, S. X. Liu, M. Zhao, and B. Teng, Experimental investigation of the hydrodynamic characteristics of heave plates using forced oscillation, Ocean Eng. **66**, 82 (2013).

[11] I. H. Cho, J.-S. Choi, and M. H. Kim, Sloshing reduction in a swaying rectangular tank by an horizontal porous baffle, Ocean Eng. **138**, 23 (2017).

[12] Q. Zang, H. Fang, J. Liu, and G. Lin, Boundary element model for investigation of the effects of various porous baffles on liquid sloshing in the two dimensional rectangular tank, Eng. Anal. Boundary Elem. **108**, 484 (2019).

[13] M.-A. Xue, Z. Jiang, P. Lin, J. Zheng, X. Yuan, and L. Qian, Sloshing dynamics in cylindrical tank with porous layer under harmonic and seismic excitations, Ocean Eng. **235**, 109373 (2021).

[14] F. Mentzoni and T. Kristiansen, Numerical modeling of perforated plates in oscillating flow, Appl. Ocean Res. **84**, 1 (2019).
[15] F. Mentzoni and T. Kristiansen, Two-dimensional experimental and numerical investigations of perforated plates in oscillating flow, orbital flow, and incident waves, Appl. Ocean Res. **97**, 102078 (2020).
[16] A. Feichtner, E. Mackay, G. Tabor, P. R. Thies, and L. Johanning, Comparison of macro-scale porosity implementations for CFD modelling of wave interaction with thin porous structures, J. Mar. Sci. Eng. **9**, 150 (2021).
[17] D. Qiao, E. Mackay, J. Yan, C. Feng, B. Li, A. Feichtner, D. Ning, and L. Johanning, Numerical simulation with a macroscopic CFD method and experimental analysis of wave interaction with fixed porous cylinder structures, Mar. Struct. **80**, 103096 (2021).
[18] A. T. Chwang, A porous-wavemaker theory, J. Fluid Mech. **132**, 395 (1983).
[19] X. Yu, Diffraction of water waves by porous breakwaters, J. Waterw. Port Coastal Ocean Eng. **121**, 275 (1995).
[20] B. Molin, F. Remy, and T. Rippol, Experimental study of the heave added mass and damping of solid and perforated disks close to the free surface, in *Proceedings of the 12th International Congress of the International Maritime Association of the Mediterranean* (Taylor & Francis, London, 2008), pp. 879–887.
[21] B. Molin and F. Remy, Experimental and numerical study of the sloshing motion in a rectangular tank with a perforated screen, J. Fluids Struct. **43**, 463 (2013).
[22] E. Mackay and L. Johanning, Comparison of analytical and numerical solutions for wave interaction with a vertical porous barrier, Ocean Eng. **199**, 107032 (2020).
[23] E. B. L. Mackay, H. Liang, and L. Johanning, A BEM model for wave forces on structures with thin porous elements, J. Fluids Struct. **102**, 103246 (2021).
[24] H. Liang, S. Zheng, A. Magee, and D. Greaves, Water wave interactions with perforated elastic disks: Quadratic pressure discharge condition, Phys. Rev. Fluids **7**, 054802 (2022).
[25] O. M. Faltinsen, *Sea Loads on Ships and Offshore Structures* (Cambridge University Press, Cambridge, 1993).
[26] M. H. Kim and D. K. P. Yue, The complete second-order diffraction solution for an axisymmetric body. Part 1. Monochromatic incident waves, J. Fluid Mech. **200**, 235 (1989).
[27] R. Eatock Taylor and J. B. Huang, Semi-analytical formulation for second-order diffraction by a vertical cylinder in bichromatic waves, J. Fluids Struct. **11**, 465 (1997).
[28] B. Teng and P. W. Cong, A novel decomposition of the quadratic transfer function (QTF) for the time-domain simulation of non-linear wave forces on floating bodies, Appl. Ocean Res. **65**, 112 (2017).
[29] J. N. Newman, Second-order, slowly-varying forces on vessels in irregular waves, in *Proceedings of the International Symposium on the Dynamics of Marine Vehicles on Structures in Waves* (University College London, London, 1974), pp. 182–186.
[30] J. A. Pinkster, Low frequency second order wave exciting forces on floating structures, Ph.D. thesis, Delft University of Technology, 1980.
[31] X. B. Chen and F. Rezende, Efficient computations of second-order low-frequency wave load, in *Proceedings of the 28th International Conference on Ocean, Offshore and Arctic Engineering* (American Society of Mechanical Engineers, Hawaii, 2009), pp. 525–532.
[32] P. W. Cong, Y. Gou, and B. Teng, A new approach to low-frequency QTF and its application in predicting slow drift force, Ocean Eng. **53**, 25 (2012).
[33] F. Zhao, T. Kinoshita, W. Bao, R. Wan, Z. Liang, and L. Huang, Hydrodynamics identities and wave-drift force of a porous body, Appl. Ocean Res. **33**, 169 (2011).
[34] J. Dokken, J. Grue, and L. P. Karstensen, Wave analysis of porous geometry with linear resistance law, J. Marine. Sci. Appl. **16**, 480 (2017).
[35] P. Cong and Y. Liu, Local enhancements of the mean drift wave force on a vertical column shielded by an exterior thin porous shell, J. Mar. Sci. Eng. **8**, 349 (2020).
[36] D. N. Konispoliatis, I. K. Chatjigeorgiou, and S. A. Mavrakos, Theoretical hydrodynamic analysis of a surface-piercing porous cylindrical body, Fluids **6**, 320 (2021).

[37] D. N. Konispoliatis, I. K. Chatjigeorgiou, and S. A. Mavrakos, Mean drift forces on a vertical porous cylindrical body, in *Proceedings of the 36th International Workshop on Water Waves and Floating Bodies* (Seoul National University, Seoul, 2021).
[38] X. B. Chen, Middle-field formulation for the computation of wave-drift loads, J. Eng. Math. **59**, 61 (2007).
[39] C. H. Lee, On the evaluation of quadratic forces on stationary bodies, J. Eng. Math. **58**, 141 (2007).
[40] H. Liang and X. B. Chen, A new multi-domain method based on an analytical control surface for linear and second-order mean drift wave loads on floating bodies, J. Comput. Phys. **347**, 506 (2017).
[41] A. T. Chwang and A. T. Chan, Interaction between porous media and wave motion, Annu. Rev. Fluid Mech. **30**, 53 (1998).
[42] B. Molin and J. P. Hairault, On second-order motion and vertical drift forces for three-dimensional bodies in regular waves, in *Proceedings of International Workshop on Ship and Platform Motions* (University of California, Berkeley, 1983), pp. 344–362.
[43] C. M. Linton and P. McIver, *Handbook of Mathematical Techniques for Wave/Structure Interactions* (Chapman and Hall/CRC, Boca Raton, FL, 2001).
[44] H. Liang, O. M. Faltinsen, and Y.-L. Shao, Application of a 2D harmonic polynomial cell (HPC) method to singular flows and lifting problems, Appl. Ocean Res. **53**, 75 (2015).
[45] Y.-L. Shao, Numerical analysis of second-order mean wave forces by a stabilized higher-order boundary element method, J. Offshore Mech. Arct. Eng. **141**, 051801 (2019).
[46] J. N. Newman, *Marine Hydrodynamics* (Massachusetts Institute of Technology Press, Cambridge, MA, 1977).
[47] H. Maruo, The drift of a body floating in waves, J. Ship Res. **4**, 1 (1960).
[48] J. N. Newman, The drift force and moment on ships in waves, J. Ship Res. **11**, 51 (1967).
[49] F. Zhao, W. Bao, T. Kinoshita, and H. Itakura, Theoretical and experimental study on a porous cylinder floating in waves, J. Offshore Mech. Arct. Eng. **133**, 011301 (2011).
[50] D. V. Evans and R. Porter, Near-trapping of waves by circular arrays of vertical cylinders, Appl. Ocean Res. **19**, 83 (1997).
[51] P. W. Cong, Y. Gou, B. Teng, K. Zhang, and Y. F. Huang, Model experiments on wave elevation around a four-cylinder structure, Ocean Eng. **96**, 40 (2015).
[52] P. W. Cong, M. Q. Zhao, B. Teng, Y. Gou, and Y. Y. Liu, Second-order near trapping of water waves by a square array of vertical columns in bi-chromatic seas, J. Fluids Struct. **121**, 103916 (2023).
[53] D.-Z. Ning, X.-L. Zhao, B. Teng, and L. Johanning, Wave diffraction from a truncated cylinder with an upper porous sidewall and an inner column, Ocean Eng. **130**, 471 (2017).
[54] M. Abramowitz and I. A. Stegun, *Handbook of Mathematical Functions: With Formulas, Graphs, and Mathematical Tables*, 55 (National Bureau of Standards, Gaithersburg, MD, 1964).
[55] A. N. Williams and W. Li, Water wave interaction with an array of bottom-mounted surface-piercing porous cylinders, Ocean Eng. **27**, 841 (2000).
[56] C. M. Linton and D. V. Evans, The interaction of waves with arrays of vertical circular cylinders, J. Fluid Mech. **215**, 549 (1990).